UNIVERSIDAD NACIONAL AUTÓNOMA DE MÉXICO

Programa de Maestría y Doctorado en Ingeniería en Energía
Procesos y Uso Eficiente de Energía

Alternatives to the Burnup Strategy and Fuel Material of the EM^2 Modular Reactor

TESIS
QUE PARA OPTAR POR EL GRADO DE:
MAESTRO EN INGENIERÍA

PRESENTA:
Ing. Manuel Emiliano Morones García

TUTOR PRINCIPAL
Dr. Juan Luis François Lacouture
Facultad de Ingeniería, UNAM

Ciudad Universitaria, Cd. Mx., diciembre 2022

JURADO ASIGNADO:

Presidente:	Dra. Cecilia Martín Del Campo Márquez
Secretario:	Dr. Armando Miguel Gómez Torres
1er. Vocal:	Dr. Juan Luis François Lacouture
2do. Vocal:	Dr. Elías Yammir García Cervantes
3er. Vocal:	Dr. Luis Carlos Juárez Martínez

Facultad de Ingeniería, Ciudad Universitaria, Ciudad de México.

TUTOR DE TESIS:

Dr. Juan Luis François Lacouture

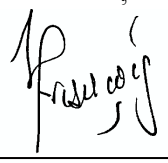

FIRMA

Acknowledgements

To the National Council of Science and Technology (CONACYT) for providing economic support for the accomplishment of this work that is part of my master's research. To the National Autonomous University of Mexico (UNAM) for its support through the research project: *Nuclear reactors and nuclear fuel cycles*, and for facilitating the use of the MIZTLI supercomputer under the LANCAD-UNAM-DGTIC-253 project.

To my tutor, Dr. Juan Luis, for his knowledge, enthusiasm, dedication, and guidance in the development of this research. To all my teachers for helping me broaden my knowledge about nuclear energy.

To my brothers, Pascual and Eloy, and my father, Eduardo, for their support during my master's studies. Lastly, a special thanks to M. Sc. Violeta, because without her wisdom, patience, and love, I would not have been able to accomplish this work.

Dedicated to Josefina, my mother

ABSTRACT

The Energy Multiplier Module (EM^2) is a modular high-temperature helium-cooled fast reactor developed by General Atomics (GA). It contemplates a convert-and-burn core, in which fertile fuel is converted to fissile fuel for on-site burning. These features allow the reactor to achieve a core lifetime of 32 years without refueling with different types of fuel materials, like thorium, natural uranium, depleted uranium (DU), and spent fuel. The objective of this research is to evaluate the performance of the EM^2 reactor under four types of fuel material combinations (Low enriched uranium [LEU]/DU, LEU/Th, U-Pu/DU and U/Th) with two burnup strategies. The first strategy was taken from the GA model (configuration 1) and the second was proposed in this thesis (configuration 2). The Serpent Monte Carlo code with ENDF/B-VII cross section library was used to perform the calculations. The following parameters were analyzed for each scenario: the effective neutron multiplication factor (*keff*), the conversion ratio, reactivity coefficients, and the effective delayed neutron fraction (β_{eff}). The fissile inventory and fission rate contribution of the main isotopes were also discussed. The results obtained show that the scenarios with configuration 2 had a higher peak excess reactivity than those with configuration 1. For the scenarios with DU as a fertile fuel, ^{238}U produced ~20% of the fission throughout the fuel cycle. In contrast, in the scenarios with thorium as fertile fuel, the ^{232}Th fission rate was negligible. As for the reactivity coefficients, all scenarios presented negative Doppler coefficient and positive void reactivity; both values increased along burnup. Furthermore, the β_{eff} decreased with burnup and did not vary significantly between both configurations.

CONTENTS

ABSTRACT v

CONTENTS vi

List of Figures viii

List of Tables x

Introduction 1

Chapter I. Small Modular Reactors 5

I.1. SMR classification 5

I.2. Generation IV Nuclear Reactors 7

I.3. Gas-cooled Fast Reactor 8

Chapter II. Energy Multiplier Module (EM^2) 12

II.1. Primary Coolant System 12

II.2. Reactor System 14

II.3. Fuel system 18

II.4. Thermal power conversion system 19

II.5. Direct reactor auxiliary cooling system 21

II.6. Fission gas collection system 21

Chapter III. Modeling and simulation of the EM^2 core 23

III.1. Core geometry 23

III.2. Material specifications 25

III.3. Reference model 26

III.4. Burnup strategy proposal 27

III.5. Alternatives fuel materials 28

III.6. Simulation methodology 30

Chapter IV. Results and discussion 31

IV.1. Reference model validation 31
IV.2. LEU/DU fuel load 34
IV.3. LEU/Th fuel load 38
IV.4. U-Pu/DU fuel load 42
IV.5. U/Th fuel load 45
Conclusions 49
References 51

List of Figures

Figure I.1. Ranges of sizes and temperatures for heat applications 7

Figure I.2. GFR with a direct Brayton cycle 9

Figure II.1. Primary coolant system of the EM^2 13

Figure II.2. Trajectory of helium in the primary system of the EM^2 13

Figure II.3. EM^2 reactor system 15

Figure II.4. EM^2 core radial distribution 15

Figure II.5. Fertile capture of ^{238}U 16

Figure II.6. Ratio of fission rates over the fuel cycle 17

Figure II.7. Evolution of the EM^2 excess reactivity 18

Figure II.8. Annular pellets and fuel rod of the EM^2 18

Figure II.9. Configuration of the EM^2 fuel assemblies 19

Figure II.10. Internal structure of the PCU 20

Figure III.1. Cross-sectional view of the EM^2 core (Serpent model) 23

Figure III.2. Serpent models for standard, reserved, and control/shutoff assemblies 24

Figure III.3. Serpent model for the fuel pellet 24

Figure III.4. Burnup strategy proposed by GA (Serpent model) 27

Figure III.5. Alternative burnup strategy (Serpent model) 28

Figure IV.1. Comparison of keff evolution 32

Figure IV.2. Total and elastic scattering cross section of ^{4}He 34

Figure IV.3. *keff* evolution of models with LEU/DU 35

Figure IV.4. Neutron spectrum of models with LEU/DU 36

Figure IV.5. Fission rate of models with LEU/DU 36

Figure IV.6. Fissile inventory change of models with LEU/DU 37

Figure IV.7. *keff* evolution of models with LEU/Th 39

Figure IV.8. Neutron spectrum of models with LEU/Th 39

Figure IV.9. Fission rate of models with LEU/Th 40
Figure IV.10. Fissile inventory change of models with LEU/Th 41
Figure IV.11. *keff* evolution of models with U-Pu/DU 42
Figure IV.12. Neutron spectrum of models with U-Pu/DU 43
Figure IV.13. Fission rates of models with U-Pu/DU 44
Figure IV.14. Fissile inventory change of models with U-Pu/DU 44
Figure IV.15. *keff* evolution of models with U/Th 46
Figure IV.16. Neutron spectrum of models with U/Th 46
Figure IV.17. Fission rate of models with U/Th 47
Figure IV.18. Fissile inventory change of models with U/Th 47

List of Tables

Table I.1. Overview of Generation IV nuclear reactors 8

Table I.2. Breed and burn reactor concepts 10

Table II.1. EM² reactor characteristics 12

Table III.1. EM² core specifications 25

Table III.2. EM² materials specifications 26

Table III.3. Reference fuels composition (mass fraction) 26

Table III.4. LEU/DU fuels composition (mass fraction) 28

Table III.5. LEU/Th fuels composition (mass fraction) 29

Table III.6. U-Pu/DU fuels composition (mass fraction) 29

Table III.7. U/Th fuels composition (mass fraction) 29

Table III.8. Density of alternative fuel materials 30

Table IV.1. Comparative table of *keff* 33

Table IV.2. Comparative table of reactivity coefficients and β_{eff} 34

Table IV.3. Discharge masses of isotopes to be recycled as U-Pu/DU fuel 38

Table IV.4. Reactivity coefficients and β_{eff} of models with LEU/DU 38

Table IV.5. Discharge masses of isotopes to be recycled as U/Th fuel 41

Table IV.6. Reactivity coefficients and β_{eff} of LEU/Th model 42

Table IV.7. Reactivity coefficients and β_{eff} of U-Pu/DU model 45

Table IV.8. Reactivity coefficients and β_{eff} of U/Th model 48

Introduction

Climate change mitigation calls for increased use of low-carbon energy technologies to achieve net-zero greenhouse gas emissions by 2050. As the United Nations Intergovernmental Panel on Climate Change (IPCC) concluded in its latest report, climate change is rapidly intensifying and demands a strong, rapid, and sustained reductions in greenhouse gas emissions (NEA, 2022). In the same way, the International Energy Agency (IEA) has stated that the path to the net-zero scenario is narrowing and will require massive deployment of all available clean energy technologies (IEA, 2020).

In this context, nuclear energy is being recognized not only as a climate-friendly energy option, but also as an enabler of the broader transformation of the energy sector (IAEA, 2021). In accordance with the IPCC, the pathways to limit average global warming to less than 1.5°C require nuclear energy to reach 1160 gigawatts of electricity by 2050 (IPCC, 2018). Similarly, the IEA projects that nuclear electricity generation will need to double between 2020 and 2050 if the world is to meet its net zero ambitions (IEA, 2021). It is important to note, however, that variable renewable energy technologies are expected to dominate the electricity mix, while nuclear power will help ensuring energy supply reliability and dispatchability.

The nuclear sector can contribute to climate change mitigation in several ways, including long-term operation of nuclear power plants, new builds of large Generation III+ nuclear reactors, and innovation in nuclear technology, such as advanced and small modular reactors (SMRs) (NEA, 2022).

In 2021, there were 437 nuclear power reactors in operation worldwide with an installed capacity of approximately 390 GWe. Of the reactors fleet, about 35% were already operating in long-term operation conditions and they contributed to avoiding the emission of 1.26 gigatons of CO_2 (PRIS, 2022). According to the Nuclear Energy Agency (NEA), long-term operation of existing reactors could save up to 49 gigatons of cumulative carbon emissions between 2020 and 2050 (NEA, 2022).

Additionally, 56 reactors with a total net capacity of 58.1 GWe were under construction in 2021 (PRIS, 2022). These new power plants will save around one gigaton of cumulative carbon emissions. But, taking into account the Generation III nuclear reactors planned, the installed capacity would raise up to 300 GWe, avoiding the emission of 23 gigatons of cumulative carbon (NEA, 2022).

As mentioned above, along with conventional nuclear power plants, new nuclear technologies could help mitigate the climate change. These are SMRs and Generation IV nuclear reactors. SMRs are nuclear reactors with power output less than 300 MWe, with some as small as 20 MWe. Their designs contemplate modular manufacturing, factory production, portability, and scalable deployment. Likewise, some SMR designs incorporate passive safety systems.

In addition to electricity production, other applications of SMRs are cogeneration for heavy industries and resource extraction, hydrogen and synthetic fuel production, desalination, and off-grid applications. Near-term deployment of SMRs could avoid 15 gigatons of carbon emissions between 2020 and 2050 (NEA, 2022).

The NEA suggests the following classification for SMR designs: single-unit light water reactor (LWR) SMRs; multi-module LWR-SMRs; mobile and transportable SMRs;

Generation IV SMRs; and microreactors (less than 20 MWe). In the first three categories, the well-established LWR technology is applied. For Generation IV SMRs, their design is based on advanced, non-LWR technologies, and include the concepts that have been investigated by the Generation IV International Forum (GIF). For microreactors, both LWR and non-LWR technologies are considered (NEA, 2022).

To summarize, with a combination of the foregoing nuclear energy applications, a total of 87 Gt of cumulative emissions would be avoided between 2020 and 2050. In this way, nuclear energy would contribute to preserving 20% of the global carbon budget consistent with a 1.5°C scenario. This would mean avoiding almost three years of global carbon emissions at 2020 levels (NEA, 2022).

Nevertheless, there are some issues to address regarding nuclear energy in the medium and long-term. First, uranium resources are limited and can support continued use of nuclear power and significant growth in nuclear capacity for over 135 years, considering uranium requirements as of 1 January 2019 (NEA/IAEA, 2020). Extracting the uranium from unconventional sources and turn it into refined uranium ready for nuclear fuel production, however, needs considerable exploration, innovative techniques and major investments.

Second, the increasing volume of nuclear waste due to the conventional approach of nuclear power. At the front end of the fuel cycle is the depleted uranium (DU), the tails product of enrichment, and at the back end of the fuel cycle is the spent nuclear fuel (SNF), the high-level waste (Schleicher et at., 2013). Regarding the DU inventory, at the end of 2018 it was estimated to amount to about 1,210,100 tons worldwide (NEA/IAEA, 2020). As for the SNF, it is accumulating at a rate of approximately 7,000 tons of heavy metal per year globally and the stored inventory is around 300,000 tons

of heavy metal (IAEA, 2022). It goes without saying that nuclear waste volume will accelerate in the upcoming years.

One way to address these issues is through Generation IV nuclear reactors, mainly fast reactors, like the Energy Multiplier Module (EM^2). The EM^2 is a passively safe, helium-cooled fast reactor currently under development by General Atomics (GA). Its core is designed to convert fertile fuel into fissile and fission it in place to accomplish a core lifetime of 32 years without refueling. The fast neutron spectrum of the reactor allows the use of various fertile materials such as DU, natural uranium, thorium, or spent fuel (Choi and Schleicher, 2017). In particular, thorium is an attractive alternative fuel, as its resources are generally 3-4 times greater than uranium resources (IAEA, 2019).

Therefore, the objective of the current research is to evaluate the performance of the EM^2 reactor under four types of fuel material combinations (Low enriched uranium [LEU]/DU, LEU/Th, U-Pu/DU and U/Th) with two burnup strategies. For this purpose, the evolution of the effective neutron multiplication factor (*keff*), the conversion ratio, the reactivity coefficients, and the effective delayed neutron fraction (β_{eff}) were compared. The Serpent Monte Carlo code (Leppänen et al., 2015) with ENDF/B-VII cross section library was used to perform the calculations.

The structure of this thesis is as follows: Chapter I presents the state of the art of the SMRs. The EM^2 modular reactor is described in Chapter II. Chapter III details the developed EM^2 models, as well as the proposed burnup strategy, alternative fuel materials, and simulation methodology. The results and comparison of the simulations with different fuel loads are analyzed in Chapter IV. Finally, the conclusions are presented.

Chapter I
Small Modular Reactors

Small Modular Reactors are nuclear reactors with power output up to 300 MWe. As their name implies, SMRs are smaller than conventional nuclear reactors in both generating capacity and physical size. In addition, their modular feature means that their systems and components can be factory-assembled and transported as a unit for installation in the desired site. Thus, SMRs can be an option to reduce cost and construction time of nuclear power plants, and for locations where the larger Generation III reactors are not suitable.

Additionally, many SMRs are designed to rely on passive systems and inherent safety characteristics of the reactor, such as low power and operating pressure. That is, in case of accident, the reactor will shut down without human intervention or backup power, since passive systems rely on physical phenomena, for example natural circulation, convection, gravity, and self-pressurization. As a result, the safety margins of SMRs with this safety approach eliminate or significantly lower the potential for releases of radioactivity to the environment (IAEA, 2021a).

I.1. SMR classification

There is a wide diversity of SMR concepts, which differ in terms of power output, operating temperature, fuel cycle, and reactor technology. The NEA suggests five categories of SMRs: single-unit LWR-SMRs; multi-modular LWR-SMRs; mobile and transportable SMRs; Generation IV SMRs; and microreactors (NEA, 2022).

- Single-unit LWR-SMRs: type of SMR that may replace small fossil-fuel power plants or be applied as distributed generation. This technology uses light water as coolant and moderator, and conventional fuels.

- Multi-module LWR-SMRs: type of SMR, with LWR technology, that may replace midsize baseload capacity or operate in a distributed generation framework.

- Mobile and transportable SMRs: type of SMR than can be easily move from one location to another. LWR technology is also used in this reactor. Floating reactors are included in this category.

- Generation IV SMRs: type of SMR that adopts advanced technologies from non-LWR reactors, such as gas-cooled fast reactor (GFR), lead-cooled fast reactor (LFR), molten salt reactor (MSR), supercritical water-cooled reactor (SCWR), sodium-cooled fast reactor (SFR), and very high temperature reactor (VHTR).

- Microreactors: type of SMR with power output up to 20 MWe especially suited for applications like electricity and process heat supplies for remote and off-grid communities and industrial locations. These SMR concepts are usually Generation IV reactors.

In general, the main application of SMRs is electricity supply. However, Generation IV SMRs can be used in a wider range of new applications, including cogeneration for heavy industries and resource extraction, hydrogen and synthetic fuel production, and desalination. Figure I.1 shows some LWR and non-LWR SMRs and the industries to

which they could supply heat. It can be seen that SMRs with GFR, liquid metal reactors (LFR and SRF), MSR, and VHTR technologies could supply heat to more industries.

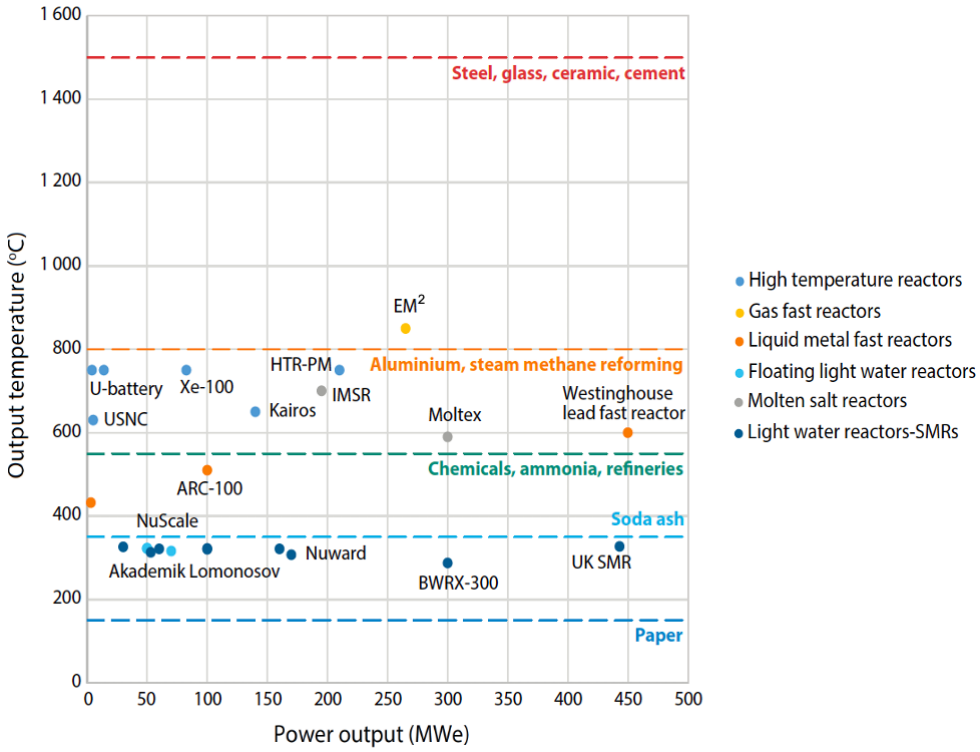

Figure I.1. Ranges of sizes and temperatures for heat applications (NEA, 2022).

Another point worth mentioning is that the EM² reactor is the reactor with the highest output temperature (850°C). In this case, the EM² design is based on the GFR concept. A description of the GFR technology is presented below.

I.2. Generation IV Nuclear Reactors

In 2002, the Generation IV International Forum (GIF) identified six nuclear energy systems that will be able to use fuel more efficiently, reduce waste production, be economically competitive, and meet stringent standards of safety and proliferation resistance (Pioro, 2016).

The six Generation IV Nuclear Reactors, selected from 130 reactor concepts, are: the gas-cooled fast reactor (GFR), lead-cooled fast reactor (LFR), molten salt reactor (MSR), supercritical water-cooled reactor (SCWR), sodium-cooled fast reactor (SFR), and very high temperature reactor (VHTR). The principal characteristics of these systems are shown in Table I.1.

Table I.1
Overview of Generation IV nuclear reactors (Pioro, 2016)

System	Neutron spectrum	Coolant	Outlet temperature [°C]	Power [MWe]
VHTR	Thermal	Helium	900-1000	250-300
GFR	Fast	Helium	850	1200
SFR	Fast	Sodium	500-550	50-150 300-1500 600-1500
LFR	Fast	Lead	480-570	20-180 300-1200 600-1000
MSR	Thermal/fast	Fluoride salts	700-800	1000
SCWR	Thermal/fast	Water	510-625	300-1500

The six systems have electricity applications. In addition, VHTR, GFR, LFR and MSR systems have potential applications in the production of hydrogen or industrial process heat for such chemical processing facilities as petroleum refineries. On the other hand, the three fast reactor systems and the MSR have the capability to transmute actinides for effective waste management (GIF, 2018).

I.3. Gas-cooled Fast Reactor

The GFR is a high-temperature helium-cooled fast spectrum reactor with an outlet temperature of 850°C. The system consider a direct Brayton cycle for power

generation, as illustrated in Figure I.2. Nevertheless, an alternative indirect cycle with a heat exchanger helium/helium-nitrogen is also contemplated. In both approaches, forced circulation is required.

The reference core consists of hexagonal fuel assemblies composed by ceramic fuel rods containing mixed carbide pellets. The high density of carbide as fuel material enhances plutonium breeding and minor actinide burning, allowing for long-term sustainability of uranium resources and waste minimization (GIF, 2018).

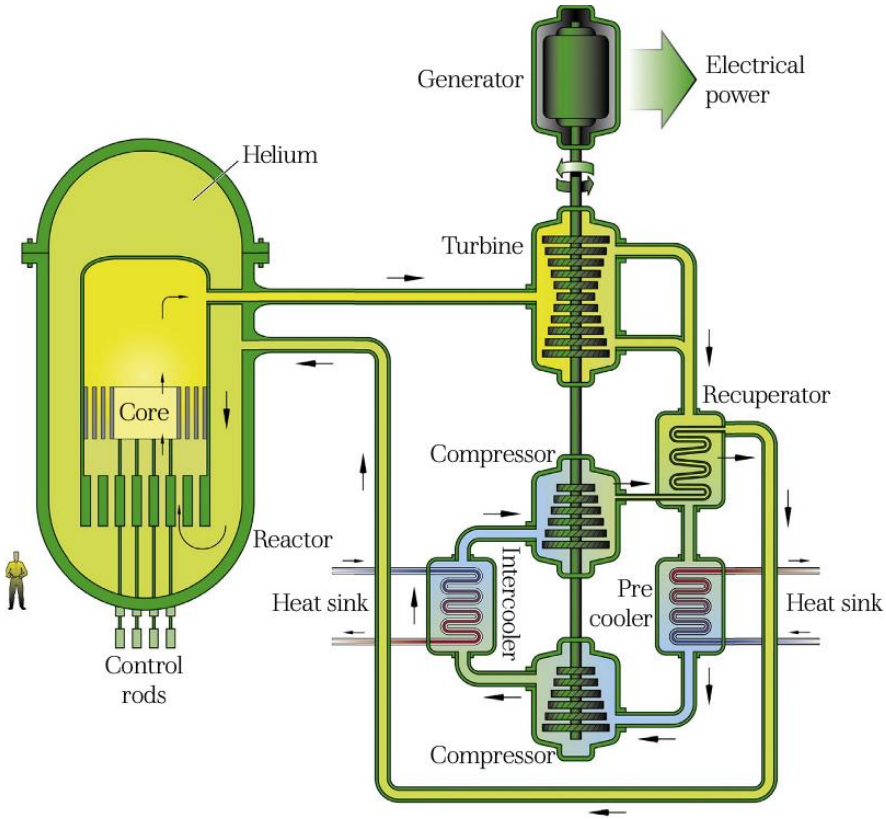

Figure I.2. GFR with a direct Brayton cycle (Pioro, 2016).

The main advantages of the GFR are:

- Higher thermal efficiency, due to the high operating temperature.
- A chemically inert, non-corrosive, single-phase coolant.

- Relatively small void reactivity coefficient (albeit positive).
- A coolant that does not dissociate nor activate.

Whereas the main drawbacks are:

- Operation under pressurized conditions.
- Low cooling efficiency of helium,
- Additional helium inventories to compensate for the loss of coolant.

It should be pointed out that GFR, and fast reactors in general, could implement the breed and burn reactor concept. This type of reactor is divided into two zones: ignition zone and breeding zone, also called blanket (Lopez-Solis and François, 2018). The ignition zone is loaded with fissile fuel, like enriched uranium or plutonium, and is where nuclear fission reactions start. Regarding the breeding zone, it is loaded with fertile fuel, such as depleted uranium, natural uranium or thorium, and is where the fertile capture reactions take place.

Table I.2
Breed and burn reactor concepts

Reactor	Type	Core life [years]	Fuel/coolant	Power [MWth]
EM²	TW	32	Carbide/He	500
ARC-100	TW	20	Metallic/Na	260
Traveling Wave Reactor (TWR)	SW	40+	Metallic/Na	1150
Fast Mixed Spectrum Reactor (FMSR)	SW	90	Metallic/Na-He	3000

There are two type of breed and burn reactor. First, there is the traveling wave (TW) reactor, where the fuel distribution is fixed and the fissions moves from the ignition

zone to the breeding zone, once it had bred fissile fuel. And second, there is the standing wave (SW) reactor, where fuel is burned and bred in different zones and then reshuffled after fissile fuel is bred in the fertile zones (Lopez-Solis and François, 2018). Table I.2 presents some examples of breed and burn reactors.

Chapter II

Energy Multiplier Module (EM^2)

The Energy Multiplier Module is a modular high temperature helium-cooled fast reactor. The EM^2 design, belonging to the generation IV of nuclear reactors, employs a direct Brayton cycle and an organic Rankine cycle for electricity generation. Each module has a thermal power of 500 MWth and can achieve an efficiency up to 53%. The general characteristics of the EM^2 are shown in Table II.1. Next, the main systems of the reactor are described.

Table II.1
EM^2 reactor characteristics

Parameter	
Power [MWth/MWe]	500/265
Coolant material	He
Coolant pressure [MPa]	13.3
Coolant inlet temperature [°C]	550
Coolant outlet temperature [°C]	850
Fuel material	UC
Cladding material	SiC-SiC

II.1. Primary Coolant System

One module of the EM^2 consists of a sealed containment formed by two chambers connected through a cross duct, as shown in Figure II.1. This structure holds the primary coolant system (PCS), integrated by the reactor system, the power conversion unit (PCU), and the direct reactor auxiliary cooling system (DRACS). In the same way, the PCS encompasses the vessel system, the inventory control system, and the helium purification system.

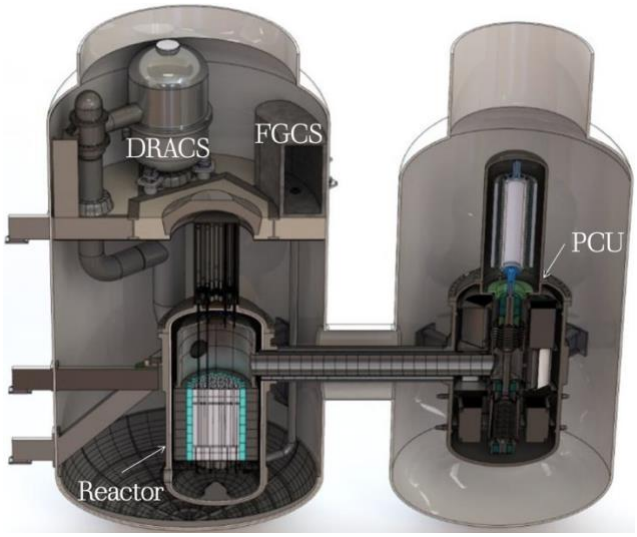

Figure II.1. Primary coolant system of the EM² (GA, 2019).

Regarding the vessel system, it is divided into two sections, the reactor vessel and the PCU vessel, connected one another by common concentric ducts. Figure II.2 points out with blue arrows the trajectory that follows the coolant in the primary system. There, it can be seen that the hot helium (850°C) flows from the core to the PCU through the inner section of the duct. When the helium reaches the turbine, it expands, pass to the recuperator and then goes to the precooler.

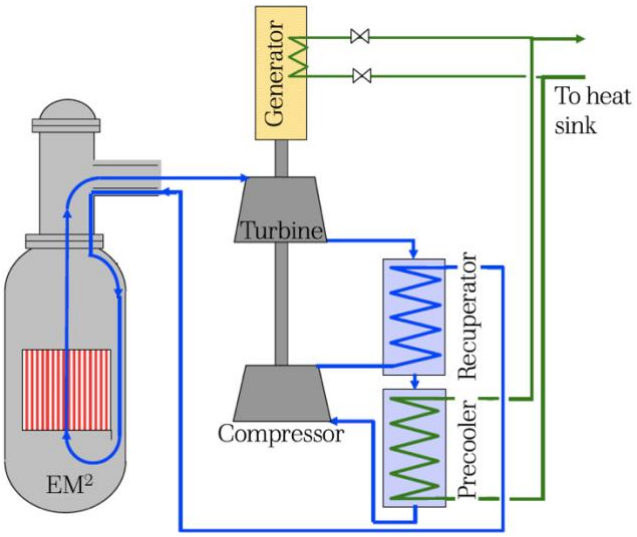

Figure II.2. Trajectory of helium in the primary system of the EM² (GA, 2019).

Subsequently, the compressor pressurizes the helium and returns it through the cold side of the recuperator. The cold helium (550°C) goes back to the reactor vessel through the annular section of the duct and flows down the outside of the core toward the lower plenum of the reactor. Finally, the helium flows up through the fuel assemblies to complete de coolant cycle. Another issue to highlight from Figure II.2 is the path, indicated in green lines, of the working fluid of the organic Rankine cycle within the primary system.

It is worth mentioning that the fission gas collection system (FGCS) is also located inside the reactor containment. This system is responsible for removing the gaseous fission products generated in the fuel and it has a direct impact in the length of the reactor operating cycle, as will be described below.

II.2. Reactor System

The reactor vessel design contemplates its manufacturing from SA-533 grade B steel plates which, despite the high coolant temperature, is a commonly used alloy in the nuclear industry. This is possible because the vessel is internally insulated with silica-alumina fibrous retained by carbon composite (C-C) plates. Likewise, a thermal shield made of C-C is placed in the vessel upper plenum to protect the top head elements from the hot helium. Figure II.3 illustrates the arrangement of the EM^2 reactor internal components.

The core is supported by the support floor through the core barrel, which is attached to the vessel below the concentric ducts. The fuel material, colored red in Figure II.3, is surrounded by a reflector composed of an inner section made of zirconium silicide

(Zr_3Si_2) and an outer section made of graphite, called primary and secondary reflectors, respectively.

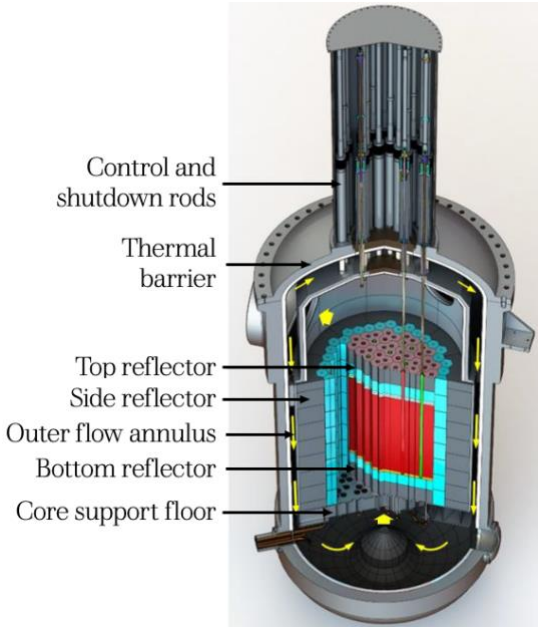

Figure II.3. EM^2 reactor system (GA, 2019).

The active core consists of 85 hexagonal fuel assemblies, of which 48 are standard assemblies, 18 control assemblies, 12 shutoff assemblies, and 7 reserved assemblies. The standard assemblies contain 91 fuel rods, while the rest contain 84 fuel rods.

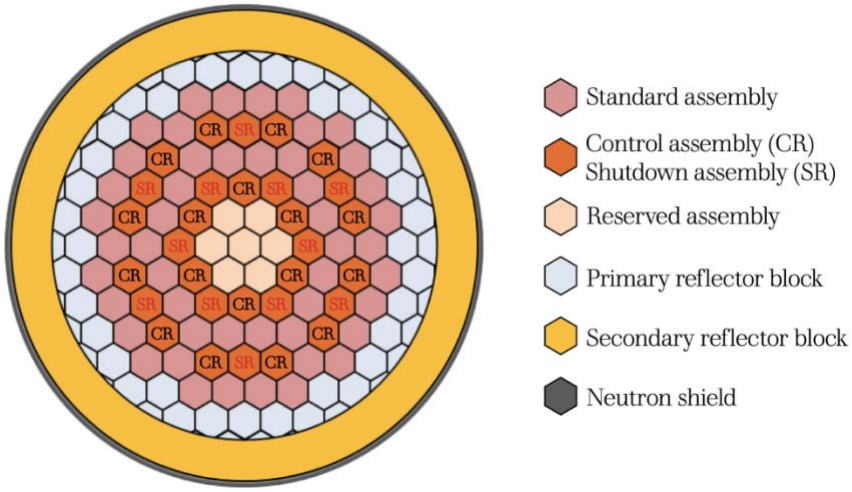

Figure II.4. EM^2 core radial distribution (Choi et al., 2020).

Both control and shutoff assemblies have a guide tube in the central area of the array. In contrast, reserved assemblies do not have any other component incorporated. The radial distribution of the fuel assemblies can be observed in Figure II.4.

According to GA, the EM^2 core has the capacity to implement the breed and burn of fuel, so it is divided into two sections, one with fissile fuel and one with fertile material. The first of these is the critical section at the beginning of core life and provides the excess of neutrons to produce new fissile material in the fertile section of the core. The fertile section is loaded with low enrichment uranium (LEU), while the fertile section is loaded with depleted uranium (DU).

The processes that take place inside the core are as follows: the ^{235}U, contained in the fissile section, is the isotope responsible for producing energy as a consequence of the nuclear fission reactions. Furthermore, it is the main contributor of positive reactivity at the beginning of fuel cycle. As stated in the previous paragraph, ^{235}U fissions supply neutrons to the fertile section for ^{238}U to be converted, by radiative capture and some intermediate beta decays, into the fissile isotope ^{239}Pu, as can be seen in Figure II.5. In addition, given the fast neutron spectrum of the reactor, the fission of ^{238}U has a non-negligible probability of occurrence, so this reaction also increases the system reactivity.

$$^{238}\mathrm{U} + \mathrm{n} \longrightarrow {}^{239}\mathrm{U} \xrightarrow{-\beta} {}^{239}\mathrm{Np} \xrightarrow{-\beta} {}^{239}\mathrm{Pu}$$

Figure II.5. Fertile capture of ^{238}U.

As ^{239}Pu is bred and starts burning, it becomes the main contributor of positive reactivity in the core. Figure II.6 shows the ratio of fission rates of ^{235}U and ^{239}Pu, the fissile isotopes, over the fuel cycle. It should be noted that the isotopes plotted do not

cover the total fissions, since approximately 20% occur in U-238. The positive reactivity added by the production of new fissile material roughly offsets the negative reactivity contributed by fission products and fuel depletion. Moreover, the FGCS constantly vents the fuel assemblies to remove gaseous fission products, thereby increasing reactivity in the core.

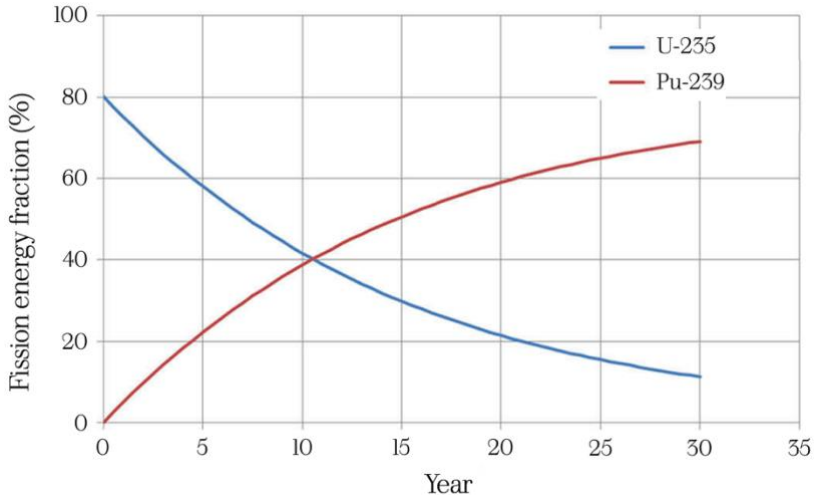

Figure II.6. Ratio of fission rates over the fuel cycle (Choi et al., 2019).

Nevertheless, the reactor becomes subcritical when fissile isotopes breeding can no longer counteract the negative reactivity of the accumulated fission products, even when the FCGS continues in operation. Figure II.7 shows the evolution of the effective neutron multiplication factor in the core. It is important to note that the reactor remains supercritical for more than 30 years.

As for the location of both fuels, Schleicher, Choi and Rawls (2013) report that the EM^2 design places the fissile material in the central region of the core and the fertile material at its axial ends. In other words, the core has a "hamburger-like" configuration where the fertile fuel performs as the buns, while the fissile fuel performs as the meat. The fissile section is radially divided into three zones with different enrichment in order to

flatten the core power distribution. According to Choi and Schleicher (2017) the initial fuel loading is 21.3 tons of fissile fuel and 19.8 tons of fertile fuel.

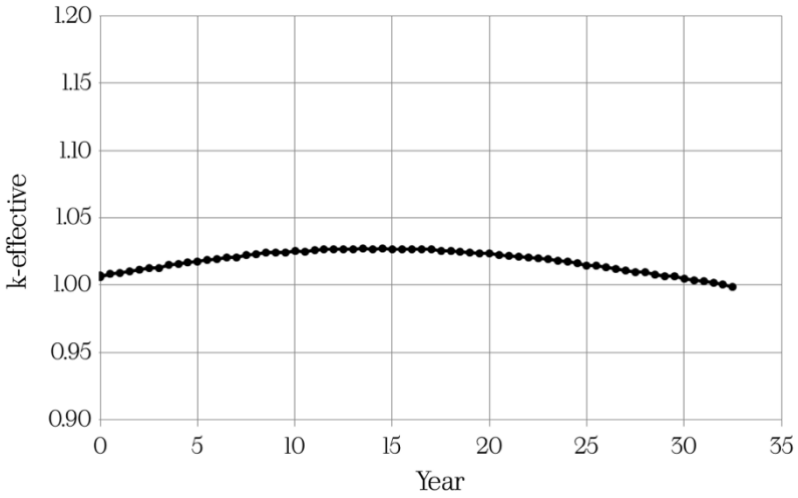

Figure II.7. Evolution of the EM^2 excess reactivity (GA, 2019).

II.3. Fuel system

The EM^2 fuel material is uranium carbide (UC) in the form of annular pellets, as shown in Figure II.8. These fuel pellets have a porosity of 25.4%; portion of its volume serves as a continuous path for the fission gases flow. Additionally, UC enables to meet the high uranium loading requirement in the core thanks to its high density. It also has the advantages of a high melting point and high thermal conductivity.

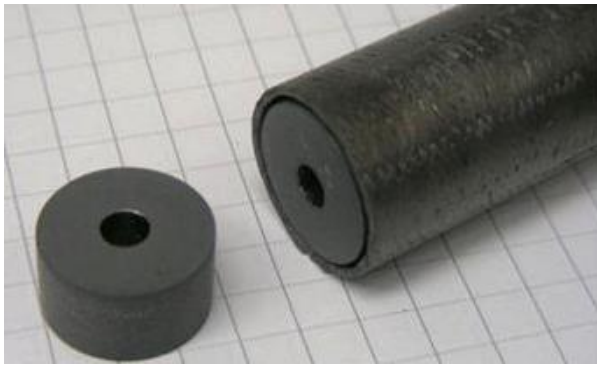

Figure II.8. Annular pellets and fuel rod of the EM^2 (Schleicher et al., 2014).

Another feature of the UC is its compatibility with the fuel rod material, SIGA™, a silicon carbide composite (SiC-SiC) patented by GA (see Figure II.8). This material is designed to preserve its stability under long-term irradiation and to withstand high temperatures. Structural components of the fuel assemblies are also considered for fabrication with this composite due to the long fuel cycle of the reactor. Figure II.9 presents the configuration of the fuel assemblies. Another point worth mentioning is the upper manifold in the assemblies, since this component collects the fission gasses that will be vented by the FGCS.

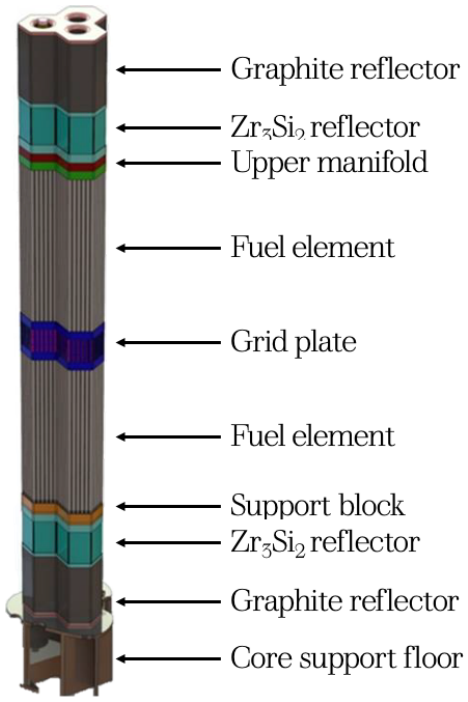

Figure II.9. Configuration of the EM^2 fuel assemblies (GA, 2019).

II.4. Thermal power conversion system

The electricity generation in this reactor technology is carried out through a combined cycle consisting of a direct Brayton cycle and an organic Rankine cycle. The first one takes place inside the PCU vessel located in the containment next to the reactor

containment and utilizes helium as the working fluid. The PCU internal structure can be seen in Figure II.10.

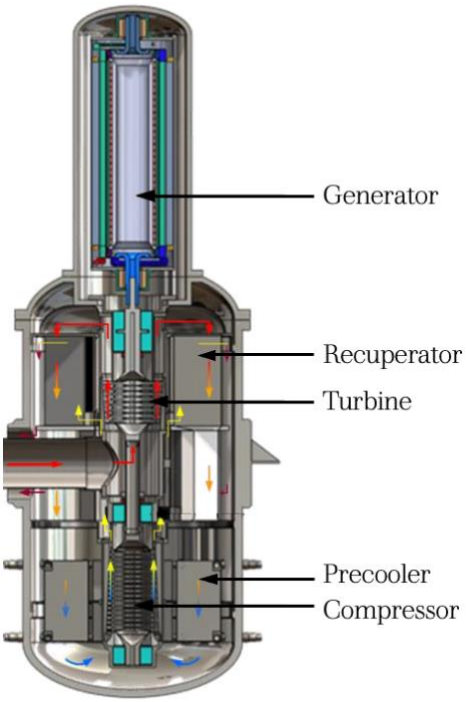

Figure II.10. Internal structure of the PCU (GA, 2019).

The generator, situated in a removable vessel for easy maintenance, uses a permanent magnet rotor in order to eliminate the Joule losses of traditional wound rotors. What is more, the generator is nonsynchronous and variable speed, which allows it to provide load following without the need to use a turbine bypass valve or to vary the helium pressure or temperature. Besides the turbo-compressor and generator, the Brayton cycle includes a helium/helium heat exchanger, the recuperator, and a helium/water heat exchanger, the pre-cooler. With respect to the organic Rankine cycle, it is located outside de reactor building and utilizes the coolant R-245fa as working fluid under supercritical conditions.

In addition, the PCU actively participates cooling the core after a reactor shutdown. In this scenario, the core residual heat enables the helium to continue to drive the turbo-compressor for a period of 20 minutes, approximately. Once this time has elapsed, the generator is put into operation as a motor to maintain primary system flow. The heat is rejected through the pre-cooler to the cooling tower.

II.5. Direct reactor auxiliary cooling system

The DRACS is the passive safety system in charge of cooling the core when the PCU is not available, either after a normal reactor shutdown or in accident conditions. A EM^2 module has two redundant loops in the DRACS with two heat exchangers in each loop. The helium flows by natural circulation to the first helium/water heat exchanger, located at the top of the reactor containment. The water that removes heat from the helium is cooled through the second water/air heat exchanger, a passive cooling tower incorporated into the reactor building.

Apart from their passive function, both DRACS loops are equipped with a circulator for active core cooling, that is, with forced helium flow. It should be added that each loop is capable of cooling the entire core.

II.6. Fission gas collection system

The FGCS functioning has an impact on reactor safety and fuel cycle length. Concerning the first aspect, this system vents the fission gasses from the fuel rods to avoid an internal overpressure that damages the rods structural integrity. The FGCS also maintains the pressure inside the fuel rods below the coolant pressure so that, in

the event of cladding failure, fission products are not released into the primary system of the reactor.

The elimination of the gaseous fission products, besides from protecting the cladding, helps to reduce the negative reactivity in the core, thus contributing to prolong the reactor core lifetime. Additionally, the FCGS reduces the source of radiation that can be released in case of an accident.

Chapter III

Modeling and simulation of the EM² core

Throughout this chapter, the developed models of the EM² core are addressed. First, the core geometry and material specifications are presented. Second, the Serpent core model that reproduce the results published by GA is described. Then, the burnup strategy proposal and the alternative fuel materials for the two burnup strategies are presented. Finally, the simulation methodology implemented in the reference model and the alternative scenarios is detailed. The Serpent Monte Carlo version 2.1.32 code with ENDF/B-VII cross section library was used to perform the depletion calculations.

III.1. Core geometry

The EM² active core consists of 85 hexagonal fuel assemblies arranged in a hexagonal lattice with a pitch of 23.281 cm. Each assembly has a support block and an upper manifold, both 10 cm high.

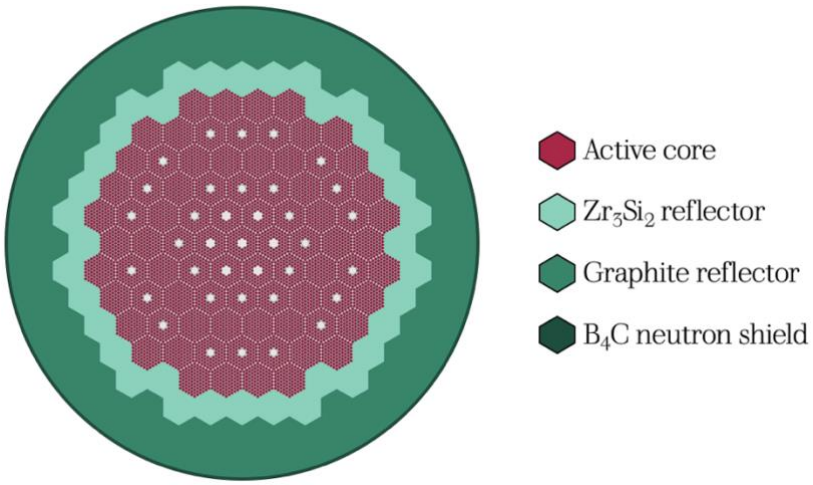

Figure III.1. Cross-sectional view of the EM² core (Serpent model).

The active core occupies a volume of 8.6 m^3 and is enclosed by the Zr_5Si_2 and graphite reflectors. In addition, the core is surrounded by a 2 cm thick boron carbide (B_4C) neutron shield. Figure III.1 shows the cross-sectional view of the Serpent core model.

There are three types of fuel assemblies in the reactor: standard, reserved, and control/shutoff (see Figure III.2). The standard assembly contains 91 fuel rods, while the reserved and control/shutoff assemblies contain 84 fuel rods.

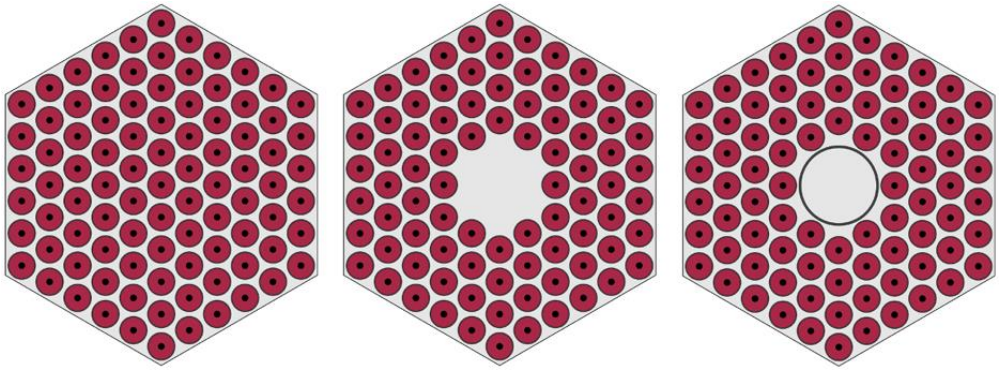

Figure III.2. Serpent models for standard, reserved, and control/shutoff assemblies.

Each fuel rod is made of uranium carbide (UC) annular pellets contained in a silicon carbide composite (SiC-SiC) cladding, as shown in Figure III.3. The fuel cladding is 2.11 cm in outer diameter and 0.95 mm thick. As for the control/shutoff assemblies guide tube, it is 3 cm in outer diameter and 2 mm thick.

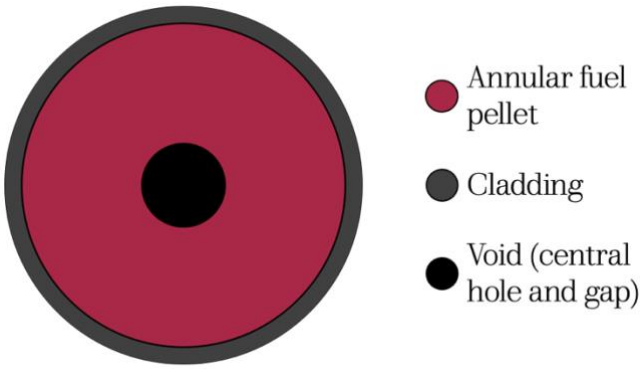

Figure III.3. Serpent model for the fuel pellet.

The annular fuel pellets have a 0.25 cm inner and 0.95 cm outer radius, resulting in a 0.01 cm fuel-cladding gap. The fuel pellets were modeled as a one-piece annular cylinder of 2.16 m heigh, i.e., without fuel-fuel gap, pellet dish, and chamfer. Apart from this, the fuel was modeled as a solid component, therefore smeared density was used. The geometrical parameters of the EM^2 core model are summarized in Table III.1.

Table III.1
EM^2 core specifications

Parameter	Value [cm]
Pellet inner radius	0.25
Pellet outer radius	0.95
Rod inner radius	0.96
Rod thickness	0.095
Rod hexagonal pitch	2.41
Guide tube inner radius	2.8
Guide tube thickness	0.2
Fuel assembly hexagonal pitch	23.281
Active core height	216
Reactor core height	316
Secondary reflector radius	172.69
Shield radius	174.69

III.2. Material specifications

Table III.2 shows the reactor core materials with their respective density. The material properties were collected from the open literature (Lemon et al., 2022; Choi et al., 2020; Jacobsen et al., 2022; Zhou et al., 2017; Höglund et al., 2012). In the reference model, UC is used as fuel material. For the alternative scenarios with thorium carbide and uranium/plutonium carbide pellets, the uranium carbide pellets porosity was applied.

Table III.2
EM^2 materials specifications

Component	Material	Density [g/cm^3]
Coolant	Helium	5.62587×10^{-3}
Fuel pellet	UC	10.18[a]
Cladding	SiC-SiC	2.8
Manifold/support block	SiC-SiC	2.8
Primary reflector	Zr_3Si_2	5.62
Secondary reflector	Graphite	1.75
Neutron shield	B_4C	2.52

[a] Smeared density of 74.7% theoretical density

III.3. Reference model

The elaboration of the reference model was carried out taking into account the data presented in Tables I.1 and III.1. Additionally, the densities of the core materials shown in Table III.2 were considered. It is worth mentioning that the grid plates were not modeled due to the lack of specifications in previous studies (Choi and Schleicher, 2017; Choi et al., 2019). Moreover, the axial reflectors, manifolds, and support blocks were assumed to be solid hexagonal blocks with a hole in the center. The control and shutoff rods were assumed to be fully withdrawn, so they were not included in the model.

Table III.3
Reference fuels composition (mass fraction)

Isotope	Fissile fuel	Fertile fuel
^{235}U	0.1102	0.0033
^{238}U	0.8417	0.9487
^{nat}C	0.0481	0.0480

Regarding the composition of the reference fuels, the fissile and fertile mass fractions are presented in Table III.3. As for the parameters to validate the reference model, the

evolution of the effective neutron multiplication factor (*keff*), conversion ratio, reactivity coefficients, and effective delayed neutron fraction (β_{eff}) were selected.

III.4. Burnup strategy proposal

As noted previously, the burnup strategy proposed by GA places the fissile material in the central region of the core and the fertile material at its axial ends, as shown in Figure III.4.

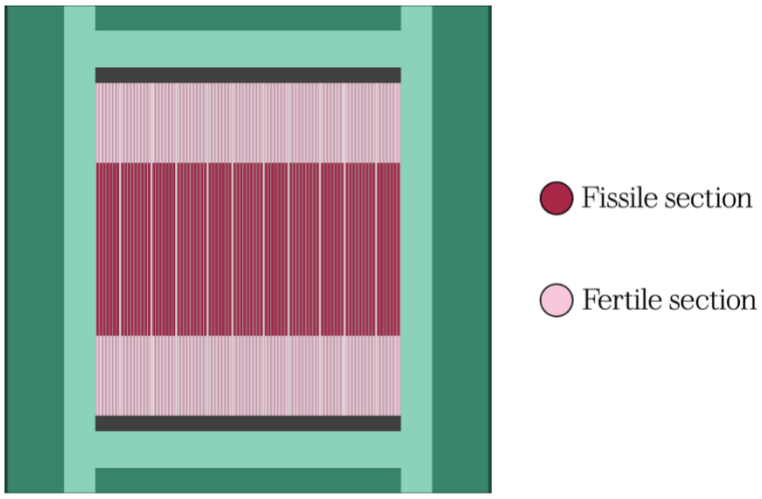

Figure III.4. Burnup strategy proposed by GA (Serpent model).

In contrast, the alternative burnup strategy was to place the fissile fuel surrounded by the fertile fuel, as illustrated in Figure III.5. For fuel assemblies containing both types of fuel materials, the volume of each was adjusted to meet the initial fuel loading of the reference model. The reference burnup strategy and the alternative burnup strategy are hereinafter referred to as configuration 1 (C1) and configuration 2 (C2) of the EM^2 core, respectively.

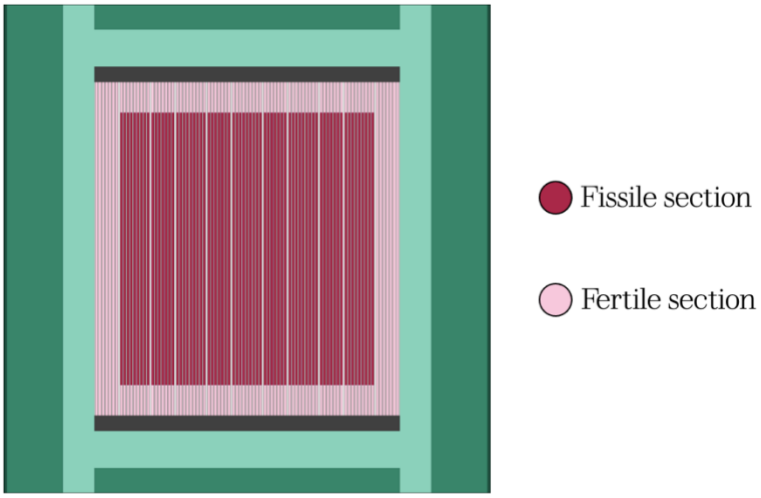

Figure III.5. Alternative burnup strategy (Serpent model).

III.5. Alternatives fuel materials

Four fissile/fertile fuel combinations were chosen as alternative fuel materials: LEU/DU, LEU/Th, U-Pu/DU, and U/Th. The LEU/DU and LEU/Th combinations were defined as the 1st generation of fuels, since their constituent isotopes can be found in nature. On the other hand, U-Pu/DU and U/Th combinations were identified as the 2nd generation, because some of their constituent isotopes were obtained from the lst generation spent fuels. The compositions of the fuel combinations are indicated in Tables III.4, III.5, III.6, and III.7.

Table III.4
LEU/DU fuels composition (mass fraction)

	Configuration 1		Configuration 2	
Isotope	Fissile fuel	Fertile fuel	Fissile fuel	Fertile fuel
^{235}U	0.1102	0.0033	0.1126	0.0033
^{238}U	0.8417	0.9487	0.8394	0.9487
^{nat}C	0.0481	0.0480	0.0481	0.0480

Table III.5
LEU/Th fuels composition (mass fraction)

	Configuration 1		Configuration 2	
Isotope	Fissile fuel	Fertile fuel	Fissile fuel	Fertile fuel
^{232}Th	-	0.9508	-	0.9508
^{235}U	0.1122	-	0.1147	-
^{238}U	0.8398	-	0.8372	-
^{nat}C	0.0481	0.0492	0.0481	0.0492

Table III.6
U-Pu/DU fuels composition (mass fraction)

	Configuration 1		Configuration 2	
Isotope	Fissile fuel	Fertile fuel	Fissile fuel	Fertile fuel
^{235}U	0.0086	0.0033	0.0086	0.0033
^{238}U	0.8478	0.9487	0.8478	0.9487
^{238}Pu	0.0011	-	0.0012	-
^{239}Pu	0.0722	-	0.0737	-
^{240}Pu	0.0200	-	0.0188	-
^{241}Pu	0.0021	-	0.0017	-
^{242}Pu	0.0003	-	0.0003	-
^{nat}C	0.0480	0.0480	0.0480	0.0480

Table III.7
U/Th fuels composition (mass fraction)

	Configuration 1		Configuration 2	
Isotope	Fissile fuel	Fertile fuel	Fissile fuel	Fertile fuel
^{232}Th	-	0.9508	-	0.9508
^{233}U	0.0482	-	0.0487	-
^{235}U	0.0316	-	0.0330	-
^{238}U	0.8722	-	0.8702	-
^{nat}C	0.0481	0.0492	0.0481	0.0492

Therefore, with four fuel combinations and two burnup strategies, a total of eight models (including the reference model) were simulated. The compositions of the fuels were adjusted so that the models had approximately the same initial *keff* as that reported by Choi et al. (2019) for the GA model. Table III.8 shows the densities of the alternatives for the EM^2 fuel material (Rodriguez and Sundaram, 1981).

Table III.8
Density of alternative fuel materials

Material	Density [g/cm^3]
$(U_{0.9}Pu_{0.1})C$	10.16
ThC	7.92

III.6. Simulation methodology

The depletion calculations were conducted with 15,000 neutrons per cycle, 500 active cycles, and 30 inactive cycles for a total of 7.5 million neutron histories; the standard deviation of the computed keff was around 20 pcm with this neutron history size. The time interval between depletion steps was set at 6 months, with smaller time steps at the beginning of the cycle, as described by Choi and Schleicher (2017).

Likewise, in every depletion step, the gaseous fission products were reduced by 70% to simulate the operation of the FGCS. However, in the absence of a list of selected fission products, elements with a boiling point equal to or lower than 900°C were reduced. For the reactivity coefficients calculation, the number of neutrons was increased to 30,000 for a total of fifteen million neutron histories, keeping the same number of cycles.

Chapter IV
Results and discussion

The parameters obtained to validate the reference model are presented in the first part of this chapter. Afterwards, the EM^2 performance results with the alternative fuel loadings are discussed. Regarding the reactivity coefficients, Doppler coefficient and void reactivity[1] were calculated considering a fuel temperature change from 1000 K to 2000 K and a helium density reduction of 99.9%, respectively (Choi and Schleicher, 2017). Both reactivity coefficients were obtained at the begging of cycle (BoC), middle of cycle (MoC), and end of cycle (EoC).

IV.1. Reference model validation

The *keff* evolution reported by GA (IAEA, 2019a) and that obtained from the reference model simulation are shown in Figure IV.1. From this comparison, it can be seen how the reference model behaved similarly to the GA model, having a root mean square deviation of 81 pcm. Table IV.1 lists the *keff* of both models and the difference between them. The largest *keff* difference was at EoC, where the reference model differed by 215 pcm from the GA model. Nevertheless, the peak excess reactivity in our model (2.64% Δk) fulfilled the ~2.7% Δk peak mentioned in Choi and Schleicher (2017).

Table IV.2 shows the reactivity coefficients and β_{eff} of GA and reference models. Overall, the values determined in this paper match those reported by Choi and Schleicher

[1] Doppler coefficient was determined with $K_D=\frac{\rho(T_2)-\rho(T_1)}{(T_2-T_1)\ln\left(\frac{T_2}{T_1}\right)}$ and void reactivity with $\alpha_v=\rho(D_2)-\rho(D_1)$.

(2017). The largest discrepancy was found in the void reactivity at EoC, where a difference of 75 pcm was registered.

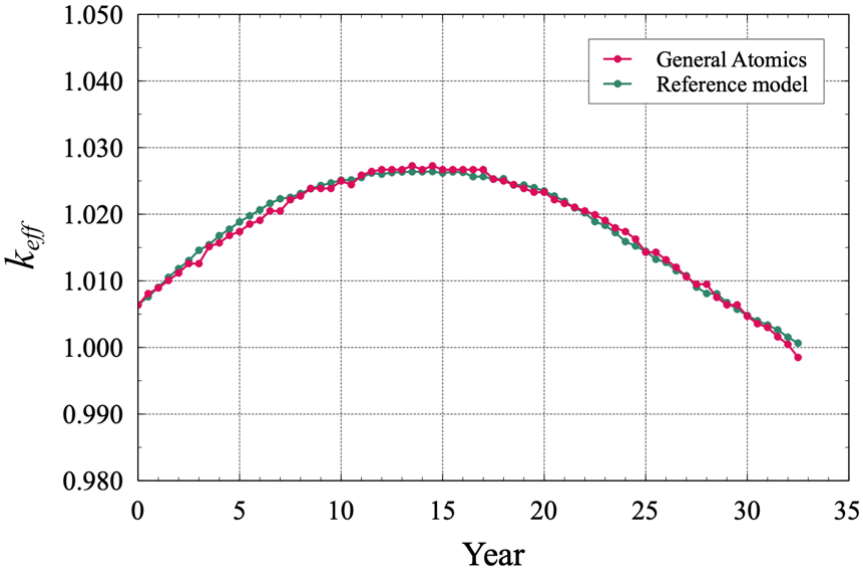

Figure IV.1. Comparison of keff evolution.

The void reactivity effect in fast reactors has two components:

1. The neutron spectrum hardening due to less neutron scattering in the coolant, in this case dominated by the elastic scattering in helium, that becomes more important towards 1 MeV, as can be seen in Figure IV.2. This spectrum hardening increases the fission probability of the main isotopes. This component has a positive reactivity effect.

2. The increased neutron leakage, due to reduced helium density, which has a negative reactivity effect.

In this case, the spectrum hardening component dominates over the neutron leakage effect.

Table IV.1
Comparative table of *keff*

Year	GA (keff)	Reference (keff ± pcm)	Difference (pcm)	Year	GA (keff)	Reference (keff ± pcm)	Difference (pcm)
0	1.00637	1.00639 ± 22	2	16.5	1.02669	1.02564 ± 21	105
0.5	1.00808	1.00761 ± 21	47	17.0	1.02669	1.02565 ± 22	104
1.0	1.00893	1.00902 ± 21	9	17.5	1.02528	1.02527 ± 21	1
1.5	1.01006	1.01053 ± 21	47	18.0	1.02500	1.02533 ± 22	33
2.0	1.01118	1.01183 ± 21	65	18.5	1.02444	1.02439 ± 23	5
2.5	1.01259	1.01304 ± 21	45	19.0	1.02387	1.02437 ± 21	50
3.0	1.01259	1.01459 ± 21	200	19.5	1.02331	1.02398 ± 21	67
3.5	1.01513	1.01542 ± 21	29	20.0	1.02331	1.02349 ± 21	18
4.0	1.01570	1.01678 ± 21	108	20.5	1.02218	1.02273 ± 20	55
4.5	1.01682	1.01775 ± 20	93	21.0	1.02162	1.02195 ± 20	33
5.0	1.01739	1.01885 ± 21	146	21.5	1.02105	1.02095 ± 21	10
5.5	1.01852	1.01976 ± 21	124	22.0	1.02049	1.02021 ± 21	28
6.0	1.01908	1.02065 ± 22	157	22.5	1.01992	1.01889 ± 21	103
6.5	1.02049	1.02163 ± 21	114	23.0	1.01908	1.01833 ± 21	75
7.0	1.02049	1.02231 ± 20	182	23.5	1.01795	1.01724 ± 21	71
7.5	1.02218	1.02253 ± 21	35	24.0	1.01739	1.01589 ± 23	150
8.0	1.02274	1.02310 ± 22	36	24.5	1.01626	1.01524 ± 21	102
8.5	1.02387	1.02383 ± 22	4	25.0	1.01429	1.01443 ± 21	14
9.0	1.02387	1.02431 ± 21	44	25.5	1.01429	1.01324 ± 21	105
9.5	1.02387	1.02469 ± 20	82	26.0	1.01316	1.01277 ± 22	39
10.0	1.02500	1.02512 ± 21	12	26.5	1.01203	1.01152 ± 20	51
10.5	1.02444	1.02515 ± 21	71	27.0	1.01062	1.01078 ± 21	16
11.0	1.02585	1.02551 ± 21	34	27.5	1.00949	1.00906 ± 22	43
11.5	1.02641	1.02618 ± 20	23	28.0	1.00949	1.00810 ± 22	139
12.0	1.02669	1.02602 ± 20	67	28.5	1.00752	1.00805 ± 21	53
12.5	1.02669	1.02625 ± 22	44	29.0	1.00639	1.00673 ± 21	34
13.0	1.02669	1.02635 ± 22	34	29.5	1.00639	1.00574 ± 20	65
13.5	1.02726	1.02637 ± 21	89	30.0	1.00470	1.00481 ± 21	11
14.0	1.02669	1.02637 ± 21	32	30.5	1.00357	1.00400 ± 20	43
14.5	1.02726	1.02640 ± 22	86	31.0	1.00301	1.00337 ± 20	36
15.0	1.02669	1.02619 ± 22	50	31.5	1.00160	1.00263 ± 21	103
15.5	1.02669	1.02636 ± 20	33	32.0	1.00047	1.00154 ± 22	107
16.0	1.02669	1.02629 ± 23	40	32.5	0.99850	1.00065 ± 21	215

Furthermore, the conversion ratio at BoC of the reference model was 1.07, which was the same value reported by GA (IAEA, 2019a). Hence, given the similar behavior of the

two models, the EM² reference model was considered verified and positively assessed against open literature information.

Table IV.2
Comparative table of reactivity coefficients and β_{eff}

	BoC		MoC		EoC	
	GA	Ref.	GA	Ref.	GA	Ref.
Doppler coefficient [pcm/K]	-1.0900	-0.9764	-0.8330	-0.7516	-0.6110	-0.6187
Void reactivity [pcm]	95.00	93.71	213.00	208.43	242.00	317.01
Effective delayed neutron fraction	0.00684	0.00696	0.00463	0.00431	0.00368	0.00369

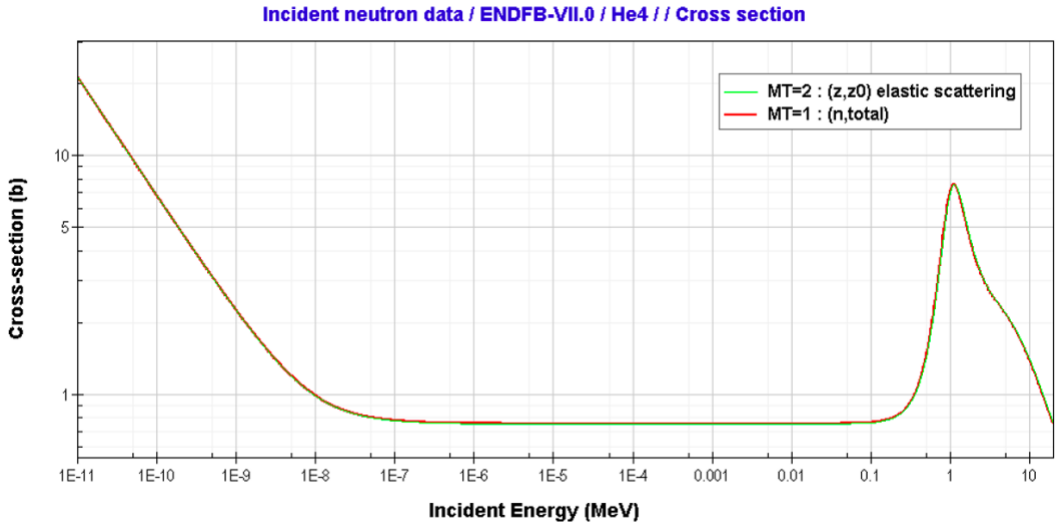

Figure IV.2. Total and elastic scattering cross section of ^{4}He.

IV.2. LEU/DU fuel load

The EM² excess reactivity for the two core configurations with LEU/DU fuel is shown in Figure IV.3. In contrast to the GA model, core configuration 2 was more reactive throughout the fuel cycle because of the distribution of the DU around the LEU. Since

the surface between the two fuels was larger, the neutron flux reached more ^{238}U in the fertile section, thus nuclear reactions increased (fast fission and fertile capture). This reactivity addition resulted in a higher *keff* peak (3.848% Δk) and the reactor continued supercritical during the 32.5-year simulation. The conversion ratio of configuration 2 was 1.16 at BoC. As expected, it was greater than the conversion ratio of configuration 1.

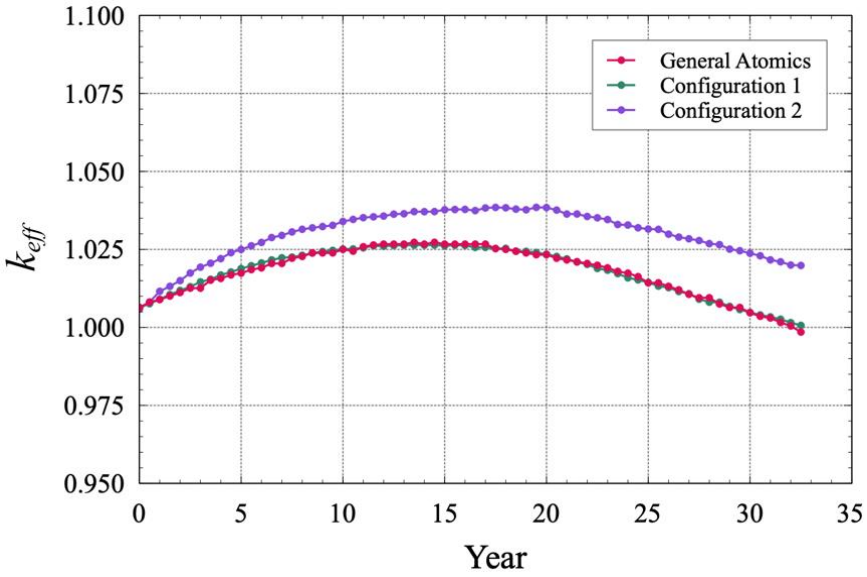

Figure IV.3. *keff* evolution of models with LEU/DU.

Additionally, the neutron spectrum was obtained for the two core configurations (see Figure IV.4). In general, both spectrums showed a typical fast reactor distribution. However, configuration 2 had a harder spectrum at BoC and MoC compared to the reference model. This means the decrease of fast neutrons over time due to the consumption of fissile isotopes, which had an impact on fast fission reactions and on breeding fissile isotopes.

Figure IV.5 shows the fission rates of the main fissile and fertile isotopes throughout the cycle. It can be observed that for the two configurations, ^{235}U was responsible for

approximately 80% of the fissions at BoC. As the burnup progressed, this fraction decreased due to uranium depletion, reaching the minimum fission rate at EoC. On the contrary, ^{239}Pu was bred over time and after ~9 years most of the reactivity came from its fission. It is worth noting that ^{238}U fast fissions produced approximately 20% of the cycle energy. Configuration 2, however, exhibited a slightly higher ^{238}U fission rate in the first half of the cycle, attributable to its harder neutron spectrum at BoC and MoC.

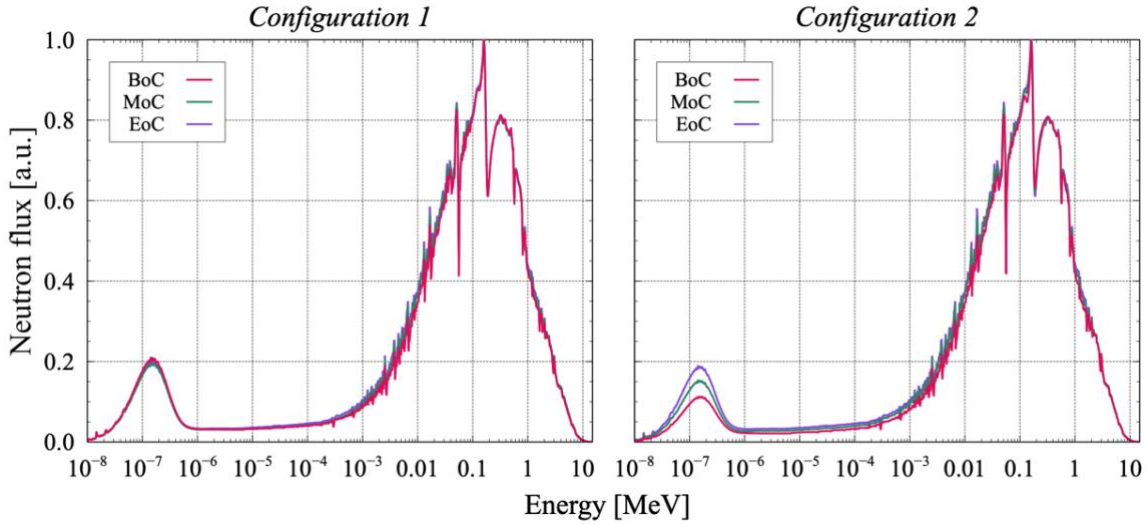

Figure IV.4. Neutron spectrum of models with LEU/DU.

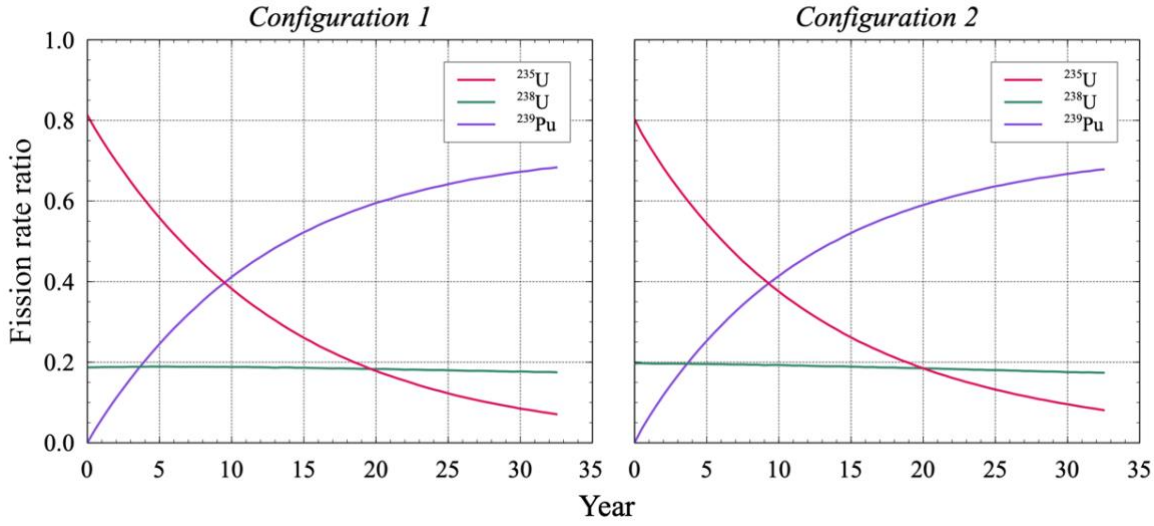

Figure IV.5. Fission rate of models with LEU/DU.

To visualize the variation of the main fissile isotopes, Figure IV.6 shows the change of the fissile inventories in the core. Again, the behavior between configurations is quite similar, but there was a faster ^{239}Pu breeding in the fertile zone of configuration 2, as well as a slower ^{235}U consumption in its fertile zone. Furthermore, for both configurations, it is noted that ^{235}U of the DU was also burned and that the highest ^{239}Pu conversion occurred in the fissile zone.

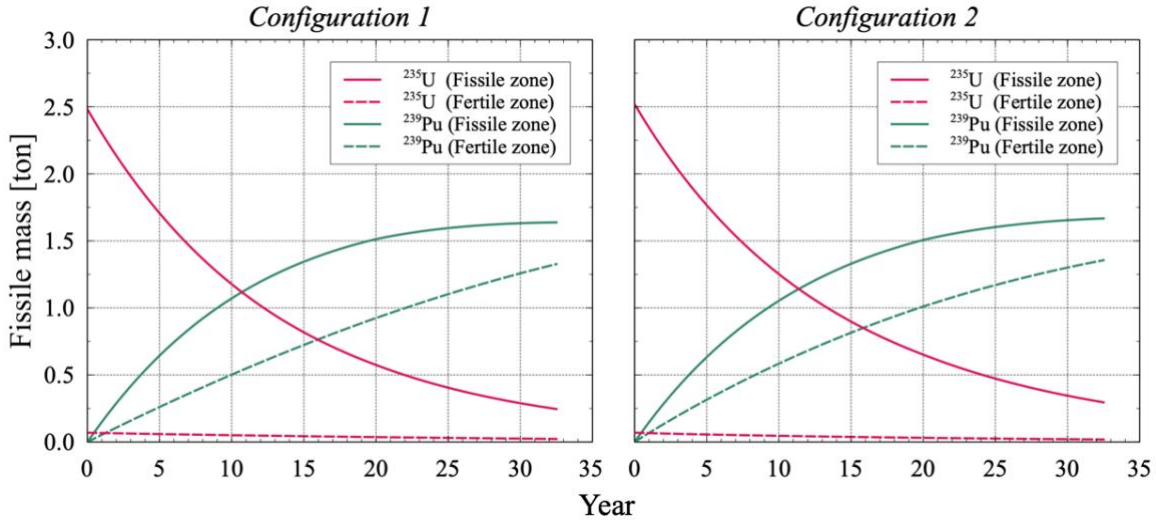

Figure IV.6. Fissile inventory change of models with LEU/DU.

As mentioned previously, LEU/DU fuel combination was classified as a first-generation fuel. Thus, in this case, uranium, and plutonium isotopes, mainly ^{235}U, ^{238}U, ^{238}Pu, ^{239}Pu, ^{240}Pu, ^{241}Pu, and ^{242}Pu, were chosen to constitute the initial fissile loading of the models with U-Pu/DU fuel (each fuel discharge/loading according to the corresponding core configuration). The discharge masses of the aforementioned isotopes are presented in Table IV.3.

Regarding the reactivity coefficients and β_{eff}, Table IV.4 shows the results obtained. Although the two scenarios followed the same tendency, given the excess reactivity of

configuration 2, this scenario resulted in higher void reactivity and less negative Doppler coefficients. The distribution of fuel materials did not affect the β_{eff}.

Table IV.3
Discharge masses of isotopes to be recycled as U-Pu/DU fuel

	Mass [kg]	
	C1	C2
^{235}U	276.5	314.3
^{238}U	31674.3	31474.6
^{238}Pu	41.3	39.9
^{239}Pu	2948.8	3022.8
^{240}Pu	572.9	591.6
^{241}Pu	48.6	49.7
^{242}Pu	7.1	7.0

Table IV.4
Reactivity coefficients and β_{eff} of models with LEU/DU

	BoC		MoC		EoC	
	C1	C2	C1	C2	C1	C2
Doppler coefficient [pcm/K]	-0.9764	-0.8462	-0.7516	-0.7122	-0.6187	-0.5836
Void reactivity [pcm]	93.71	97.75	208.43	280.49	317.01	333.36
Effective delayed neutron fraction	0.00696	0.00722	0.00431	0.00433	0.00369	0.00377

IV.3. LEU/Th fuel load

The EM^2 *keff* behavior for the two core configurations with LEU/Th fuel is shown in Figure IV.7. It can be noticed that configuration 1 was less reactive compared to the GA model, even the reactor became subcritical after 27 years. On the other hand, configuration 2 was more reactive and the core remained supercritical throughout the fuel cycle (the difference between the *keff* behavior of the two configurations was

discussed above). Their respective excess reactivity peaks were 2.259% Δk and 3.576% Δk. In addition, the neutron spectrums for this fuel combination showed practically the same distribution as the models with LEU/DU fuel (see Figure IV.7). The conversion ratios at BoC were 1.06 and 1.13 for the first and second configurations, respectively.

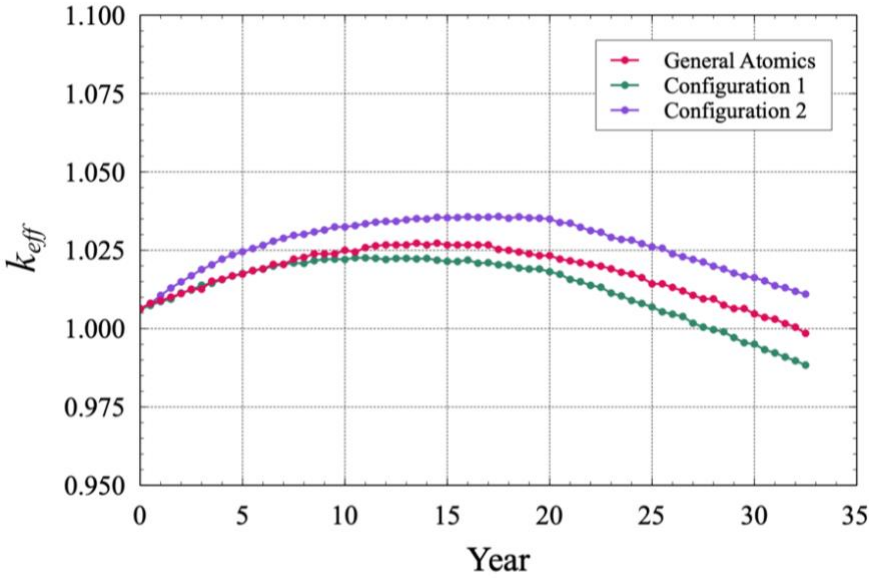

Figure IV.7. *keff* evolution of models with LEU/Th.

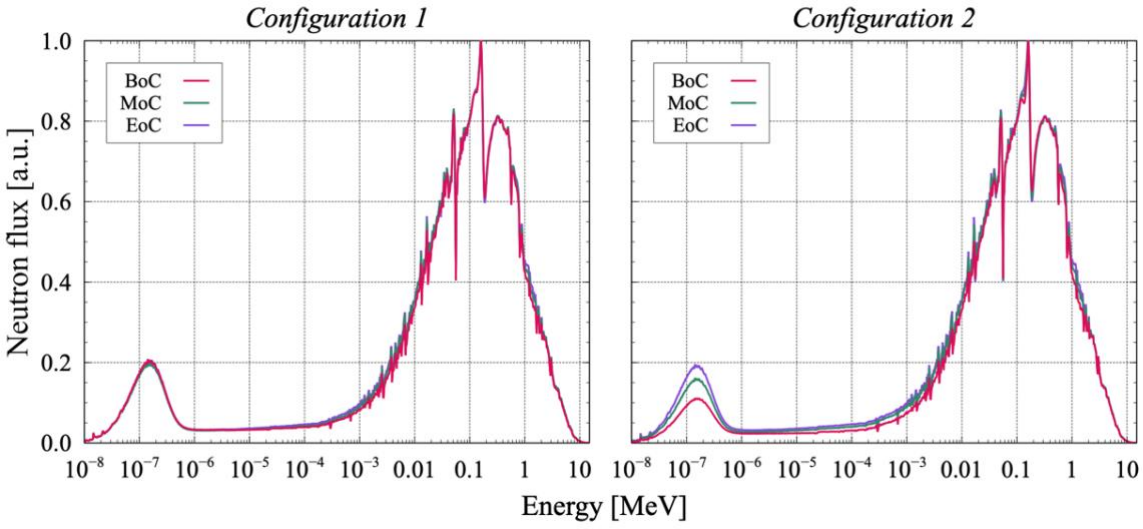

Figure IV.8. Neutron spectrum of models with LEU/Th.

As observed in Figure IV.7, in general, LEU/Th fueled models were less reactive compared to the LEU/DU fueled models as a result of the substitution of DU for thorium. Firstly, because ^{232}Th has a smaller fission cross section than ^{238}U, so its fissions at a slower rate. It can be seen from Figure IV.9 that the ^{232}Th fission rate was almost zero during the whole cycle. In contrast, ^{238}U generated about 17.5% of the energy at BoC and dropped to 11.5% at EoC, and neither the fission rates of ^{239}Pu nor ^{233}U were sufficient to offset this reduction in reactivity. Apart from this, a faster ^{233}U fission rate is appreciated in configuration 2, along with a lower energy contribution from ^{239}Pu and ^{235}U throughout the cycle.

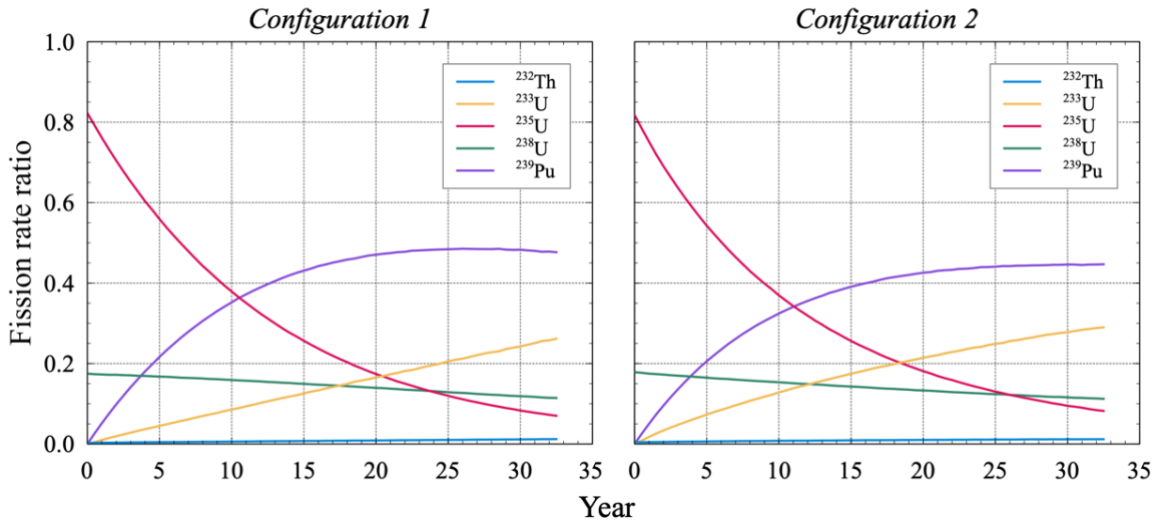

Figure IV.9. Fission rate of models with LEU/Th.

Secondly, ^{233}U breeding, and therefore its fission rate, was not faster enough. Unlike DU, thorium did not burn enough to provide extra neutrons in the fertile section to breed fissile isotopes. The fissile inventory for configurations 1 and 2 is shown in Figure IV.10. In both cases, the conversion of ^{233}U was slower compared to the conversion of ^{239}Pu in the fertile section of models with LEU/DU fuel. Additionally, there was a minimum production of ^{235}U in the fertile section, noticeable at EoC.

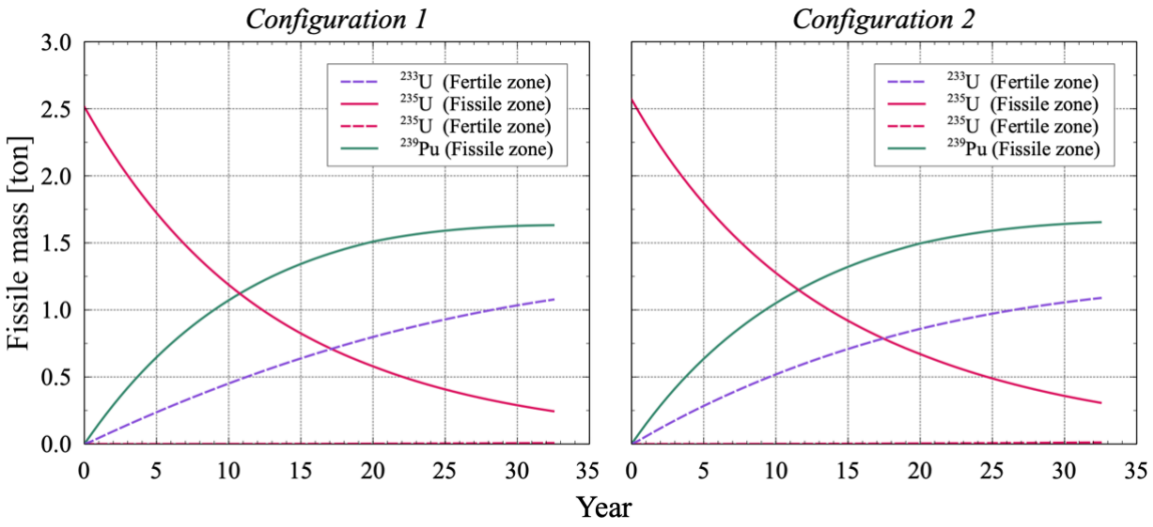

Figure IV.10. Fissile inventory change of models with LEU/Th.

This fuel combination was classified as a first-generation fuel as well. Thus, the isotopes ^{233}U, ^{235}U, and ^{238}U were chosen to constitute the initial fissile loading of the models with U/Th fuel. Table IV.5 presents the discharge masses of these isotopes.

Table IV.5
Discharge masses of isotopes to be recycled as U/Th fuel

	Mass [kg]	
	C1	C2
^{233}U	1077.1	1088.8
^{235}U	252.0	319.1
^{238}U	14123.7	14300.4

As for the reactivity coefficients (see Table IV.6), Doppler coefficients were less negative as the burnup increased due to the ^{238}U consumption, just like in the LEU/DU fuel loading scenarios, but at a slower rate. For the void reactivity and the β_{eff}, they resulted similar for the two configurations at BoC, MoC, and EoC. Moreover, the substitution of DU for thorium did not affect the resulting β_{eff}, as these results matched those of the LEU/DU scenarios.

Table IV.6
Reactivity coefficients and β_{eff} of LEU/Th model

	BoC		MoC		EoC	
	C1	C2	C1	C2	C1	C2
Doppler coefficient [pcm/K]	-0.8912	-0.8733	-0.7290	-0.7533	-0.6633	-0.6639
Void reactivity [pcm]	46.40	45.40	210.22	203.74	293.55	287.26
Effective delayed neutron fraction	0.00704	0.00704	0.00430	0.00442	0.00362	0.00368

IV.4. U-Pu/DU fuel load

The U-Pu/DU load, a second-generation fuel, used recycled fuel as fissile material and DU as fertile material. The EM² *keff* behavior for the two core configurations with U-Pu/DU fuel is shown in Figure IV.11.

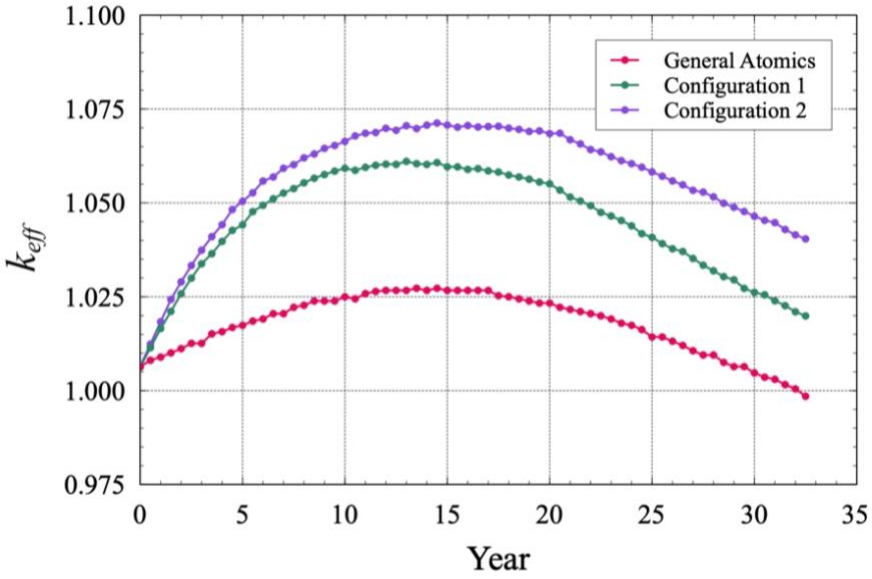

Figure IV.11. *keff* evolution of models with U-Pu/DU.

It is clear that the models with this fuel combination were more reactive than the GA model. In fact, this scenario was the most reactive of all, reaching excess reactivity

peaks of 6.105% Δk and 7.126% Δk, respectively. Likewise, the conversion ratios were the highest registered (CR=1.56 for configuration 1 and CR=1.67 for configuration 2). Nevertheless, the neutron spectra followed the same distribution as the previous scenarios, as seen in Figure IV.12.

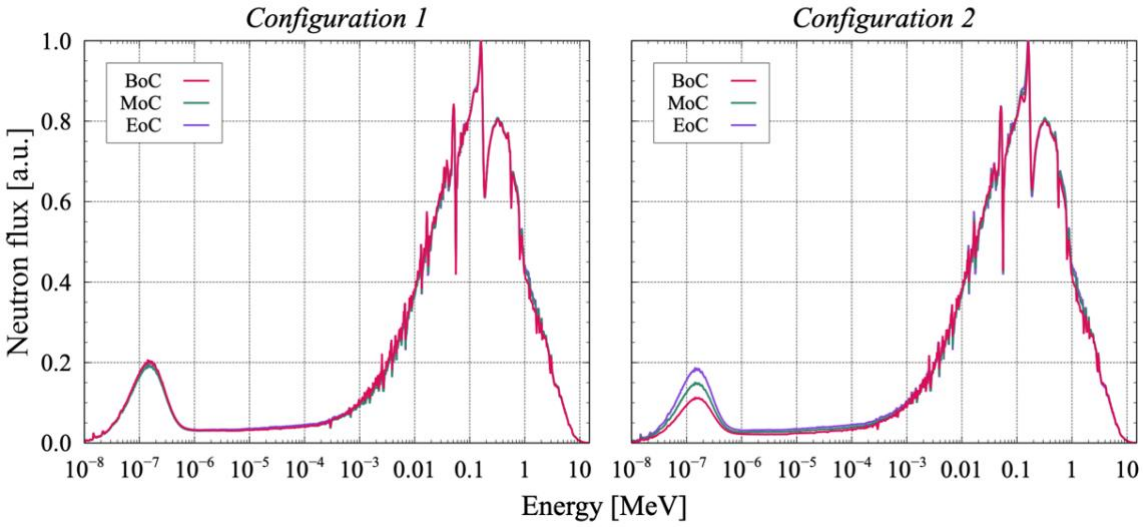

Figure IV.12. Neutron spectrum of models with U-Pu/DU.

The reactivity gain of this scenario was caused by the presence of ^{239}Pu in the core since this isotope is more reactive than ^{235}U. Figure IV.13 shows the fission rates for the two configurations. It is observed that the two models behave in a similar way, with configuration 2 being more reactive. In both cases, the ^{239}Pu began generating about 60% of the energy and ended the cycle exceeding 70%. It is noteworthy that the fast fissions of ^{238}U were the second energy source of the cycle. Additionally, it stands out that the fission rates of ^{240}Pu and ^{241}Pu were higher than those of ^{235}U in the second half of the cycle.

Moreover, unlike ^{235}U in the LEU fuel cases, whose mass decreased with time, the mass of ^{239}Pu increased in the fissile section of both configurations, reaching a maximum around year 20 (see Figure IV.14). In other words, in the fissile section of this scenario,

^{239}Pu was bred at a higher rate than it was burned in the first 20 years of the fuel cycle. After this period, the burn rate dominated. At EoC, in the fissile section of the core, there was more ^{239}Pu than at BoC. Regarding the fertile section, uranium and plutonium followed the same evolution as in the LEU/DU fueled models.

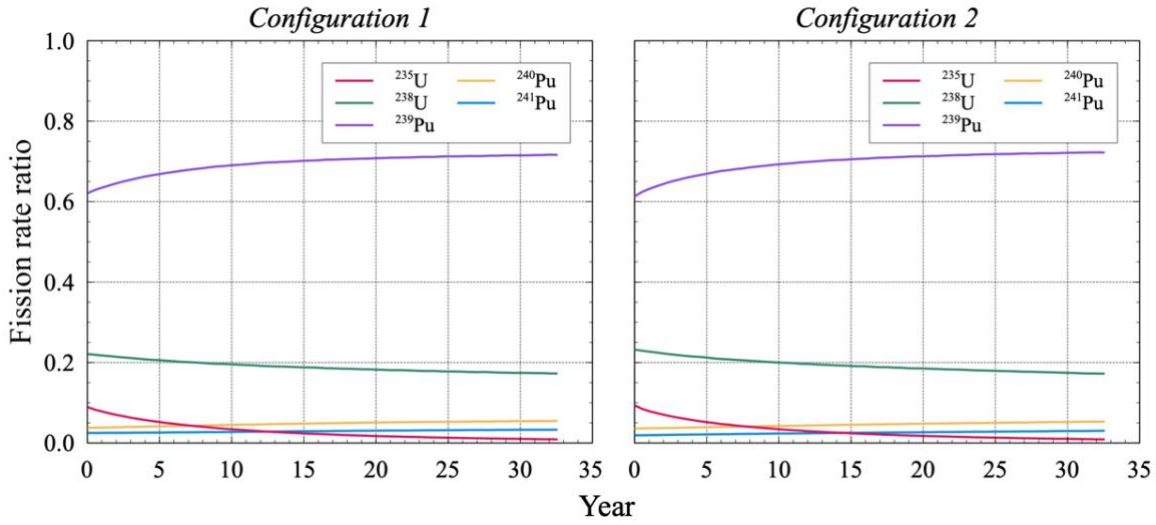

Figure IV.13. Fission rates of models with U-Pu/DU.

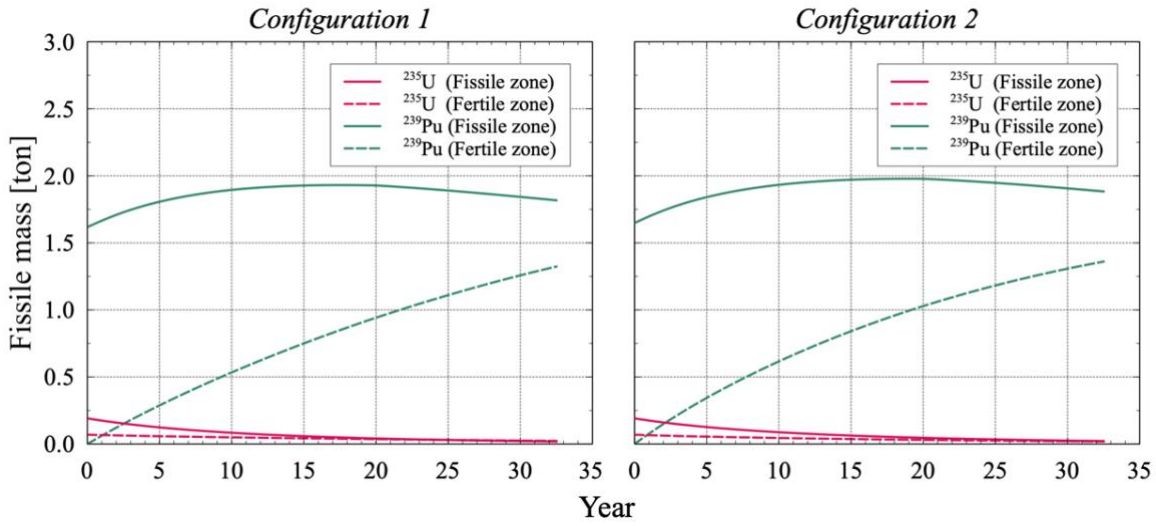

Figure IV.14. Fissile inventory change of models with U-Pu/DU.

The reactivity coefficients obtained from this pair of models reflected how reactive the core was. Doppler coefficients became less negative at a faster rate compared to the

rest of the models, while void reactivity presented the highest values (see Table IV.7). In addition, the resulting β_{eff} were the lowest calculated, as ^{239}Pu has a lower β_{eff} than ^{235}U. Taking everything into account, the core with this fuel combination would be the most difficult to control in reactivity-induced transients.

Table IV.7
Reactivity coefficients and β_{eff} of U-Pu/DU model

	BoC		MoC		EoC	
	C1	C2	C1	C2	C1	C2
Doppler coefficient [pcm/K]	-1.0021	-0.9480	-0.6044	-0.6031	-0.5403	-0.5711
Void reactivity [pcm]	263.99	211.80	317.31	323.42	367.94	363.70
Effective delayed neutron fraction	0.00418	0.00432	0.00349	0.00355	0.00356	0.00342

IV.5. U/Th fuel load

In the same way as the last fuel combination, U/Th load is a second-generation fuel, so it used recycled fuel as the fissile material and thorium as the fertile material; ^{235}U was added to the fissile fuel to meet the initial reference *keff*. The EM^2 *keff* behavior for the two core configurations with U/Th fuel is shown in Figure IV.15. It can be observed that for both configurations, the *keff* decreased in the first years of depletion. After reaching a minimum, reactivity was added to the system and the *keff* started to increase, achieving excess reactivity peaks of 1.425% Δk in configuration 1 and 2.853% Δk in configuration 2.

The conversion ratio for each configuration was 1.28 and 1.37, respectively. Concerning the neutron spectra, as shown in Figure IV.16, they presented the same distribution as the other models, although at MoC, configuration 2 had a softer spectrum.

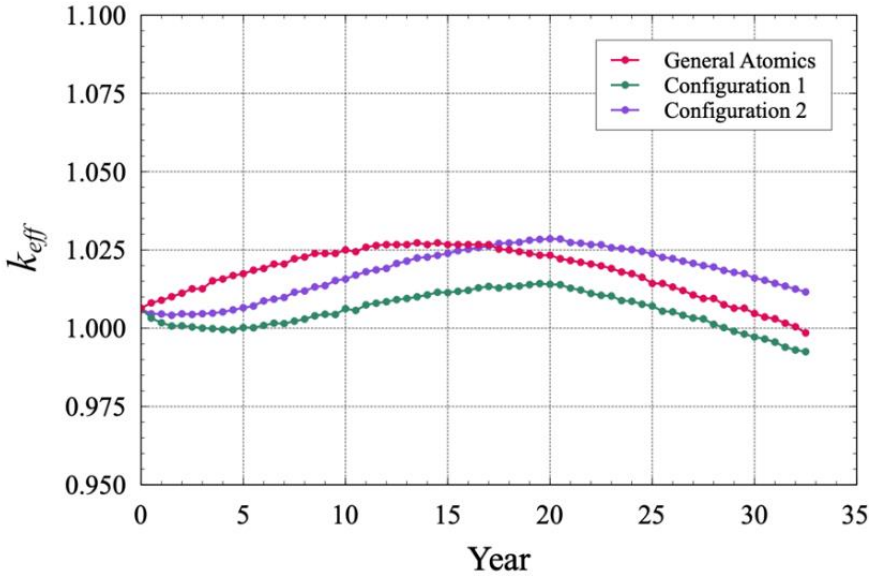

Figure IV.15. *keff* evolution of models with U/Th.

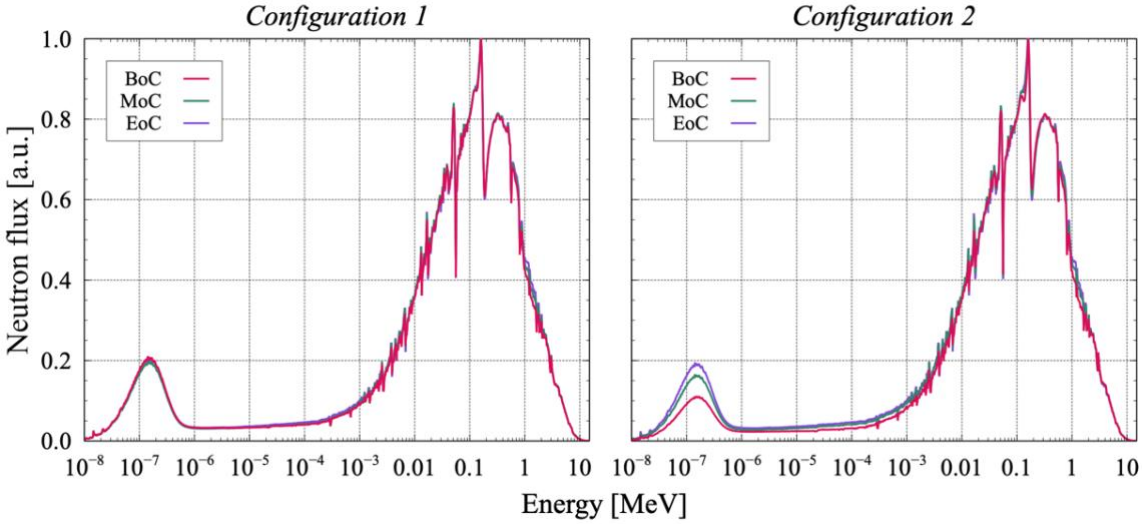

Figure IV.16. Neutron spectrum of models with U/Th.

The fission rates throughout the fuel cycle of the U/Th fueled models are shown in Figure IV.17. It can be observed that ^{233}U was the main provider of positive reactivity at BoC. As burnup started, the ^{233}U fission rate dropped due to the uranium depletion. This reduction in fission was not offset by ^{235}U or ^{239}Pu fission in the first five years, nevertheless, as ^{239}Pu was bred, its fission increased, replacing ^{233}U as the principal energy generating isotope. The ^{233}U fission rate drop was counteracted by the

conversion of ^{232}Th to ^{233}U in the fertile section of the core (see Figure IV.18). It should be added that the fast fissions of ^{238}U were the third most important provider of positive reactivity in the core.

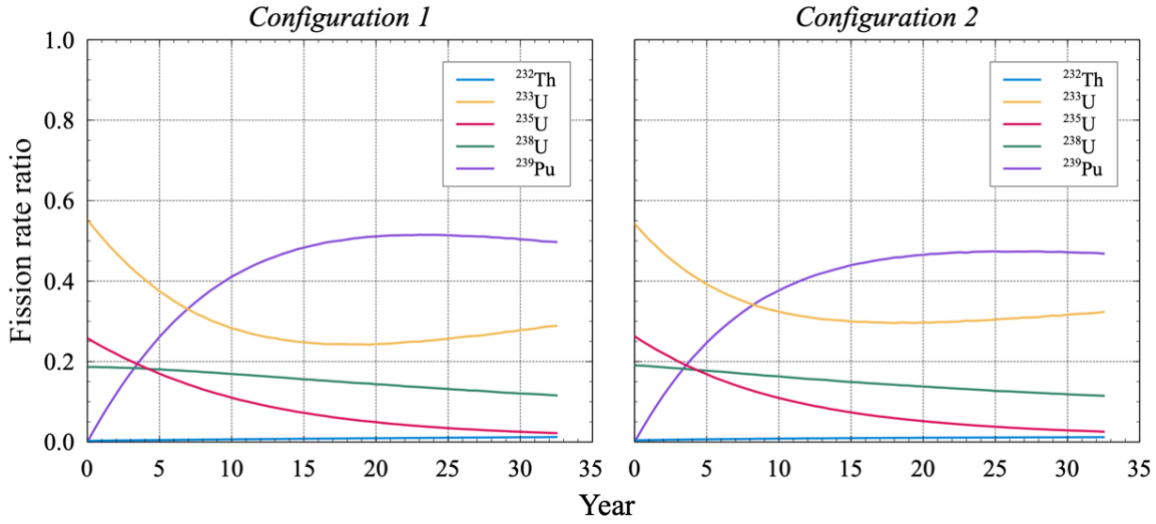

Figure IV.17. Fission rate of models with U/Th.

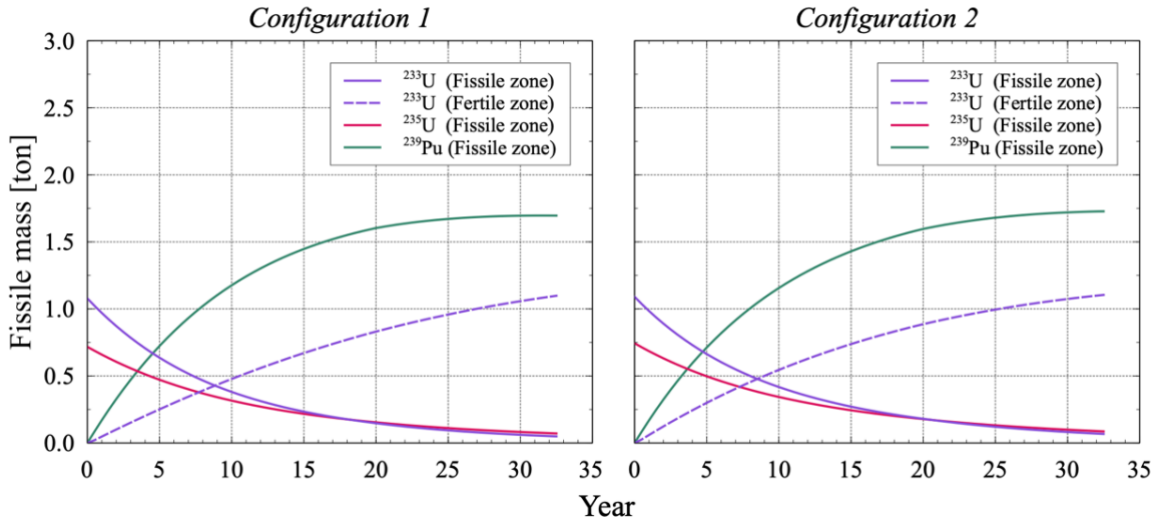

Figure IV.18. Fissile inventory change of models with U/Th.

Figure IV.18 also shows the rapid consumption of ^{233}U in the fissile section. At EoC, approximately the same amount of ^{235}U and ^{233}U remained. Regarding the ^{233}U in the fertile zone, even though its breeding rate in configuration 2 was faster, in both

configurations it ended up with a mass of ~1.1 tons. Furthermore, considering the two fuel zones, the total mass of ^{233}U was greater at EoC than in the initial fuel load.

Doppler coefficients, void reactivity, and the β_{eff} of the models with U/Th fuel are shown in Table IV.8. At BoC, this scenario obtained the most negative Doppler coefficients for both configurations. As for the void reactivities, these increased rapidly with time due to the ^{239}Pu and ^{233}U breeding, meaning that the fission reaction positive effect largely exceeded the negative neutron leakage effect. And for the β_{eff}, they were similar to those shown by the models with U-Pu/DU fuel, but with higher values at BoC, because ^{233}U has a higher β_{eff} than ^{239}Pu.

Table IV.8
Reactivity coefficients and β_{eff} of U/Th model

	BoC		MoC		EoC	
	C1	C2	C1	C2	C1	C2
Doppler coefficient [pcm/K]	-1.1058	-1.1236	-0.7702	-0.7727	-0.6079	-0.6798
Void reactivity [pcm]	53.30	69.09	261.92	270.40	332.43	331.51
Effective delayed neutron fraction	0.00526	0.00527	0.00364	0.00391	0.00339	0.00350

Conclusions

The EM^2 reference model developed in this paper reproduced the results of simulations performed by GA (2019) and Choi and Schleicher (2017) with good accuracy. The root mean square deviation between the reference model and the GA model for the *keff* evolution was 81 pcm. To achieve a smaller error, a more detailed description of the reactor core is required.

Regarding the alternative fuel materials, in the scenarios with thorium as the fertile fuel and configuration 1 as the burnup strategy, the reactor became subcritical before 32 years, failing to meet the cycle length requirement proposed by GA. However, with configuration 2 as the burnup strategy, the reactor remained supercritical throughout the fuel cycle. That is, in case of implementing any of the configuration 2 scenarios with thorium, it will not be necessary to add positive reactivity to the system. In particular, the U/Th fuel combination seems to be the more attractive option, since its peak excess reactivity is similar to that of the GA model.

Another point worth mentioning about the scenarios with thorium is that the accumulated plutonium at EoC is lower compared to the LEU/DU and U-Pu/DU scenarios, thus the risk of proliferation is lessened. As for the U-Pu/DU scenarios, they produced the largest amount of fissile material. Their initial load of plutonium was not consumed. Moreover, these scenarios were the most reactive, as reflected by their reactivity coefficients. Further studies should be performed to evaluate the reactor shutdown margin with the U-Pu/DU loading.

For all simulated scenarios, Doppler coefficients were negative and void reactivities were positive. In both cases, their values increased with burnup (Doppler less negative, void more positive). From the safety point of view, the EM^2 core design could be improved to avoid positive void reactivity, which would facilitate the control of the reactor, mainly in the event of a transient or an accident. The LEU/Th scenarios showed the lowest void reactivity coefficient, primarily due to the high thorium content.

It is worth mentioning that most of the fuel materials considered in this work require further research and development, since the only pellet that has been fabricated by GA is uranium carbide. In addition to this, the technologies considered for fuel reprocessing also require further development in order to fabricate pellets of recycled materials (Choi and Schleicher, 2017).

As for the β_{eff}, it decreased with burnup in all scenarios as fertile fuel was consumed and fissile isotopes were produced. This behavior also contributes to the core being more difficult to control over time. Furthermore, this parameter did not vary significantly between burnup configurations.

According to the mass resulting from the scenarios loaded with 2nd generation fuel, it can be concluded that a new reactor fleet could be fueled with a 3rd generation fuel. In this way, it would be possible to continue with the closed fuel cycle contemplated for this reactor technology and, consequently, with the reduction of radioactive waste.

References

Choi, H., & Schleicher, R. W. (2017). The energy multiplier module (EM^2): Status of conceptual design. *Nuclear Technology*, *200*(2), 106–124. https://doi.org/10.1080/00295450.2017.1364064.

Choi, H., Choi, M., & Hon, R. (2019). Benchmarking DRAGON/PARCS Against KRITZ and FFTF Measurements. *Nuclear Technology*, *205*(3), 486–505. https://doi.org/10.1080/00295450.2018.1495001.

Choi, H., Schleicher, R. W., & Bolin, J. (2020). Performance Analysis of Silicon Carbide Composite Clad Uranium Carbide Fuel for a Long-Life Gas-Cooled Fast Reactor Under Normal Operation—Part I: Design Criteria and Material Data. *Nuclear Technology*, *206*(7), 993–1009. https://doi.org/10.1080/00295450.2019.1698936.

GIF (2018). *GIF R&D Outlook For Generation IV Nuclear Energy Systems: 2018 Update*. https://www.gen-4.org/gif/jcms/c_196887/gif-r-d-outlook-for-generation-iv-nuclear-energy-systems-2018-update-new-cover.

Höglund, C., Birch, J., Andersen, K., Bigault, T., Buffet, J.-C., Correa, J., van Esch, P., Guerard, B., Hall-Wilton, R., Jensen, J., Khaplanov, A., Piscitelli, F., Vettier, C., Vollenberg, W., & Hultman, L. (2012). B_4C thin films for neutron detection. *Journal of Applied Physics*, *111*(10), 104908. https://doi.org/10.1063/1.4718573.

IAEA (2019). *World Thorium Occurrences, Deposits and Resources (IAEA-TECDOC-1877)*. https://www.iaea.org/publications/13550/world-thorium-occurrences-deposits-and-resources.

IAEA (2019a). *Status Report - EM^2 (General Atomics)*. https://aris.iaea.org/PDF/EM2(GeneralAtomics)_2020.pdf.

IAEA (2020). *Advances in Small Modular Reactor Technology Developments*. https://aris.iaea.org/Publications/SMR_Book_2020.pdf.

IAEA (2021). *Nuclear Energy for a Net Zero World*. www.iaea.org/resources/brochure/nuclear-energy-for-a-net-zero-world.

IAEA (2021a). *Technological Roadmap for Small Modular Reactor Deployment*. https://www-pub.iaea.org/MTCD/Publications/PDF/PUB1944_web.pdf.

IAEA (2022). *Nuclear Technology Review, 2022*. https://www.iaea.org/sites/default/files/gc/gc66-inf4.pdf.

IAEA/NEA (2020). *Uranium 2020: Resources, Production and Demand*. OECD Publishing. https://doi.org/10.1787/d82388ab-en.

IEA (2020). *World Energy Outlook 2020*. www.iea.org/reports/world-energy-outlook-2020.

IEA (2021). *Net Zero by 2050: A Roadmap for the Global Energy Sector*. www.iea.org/reports/net-zero-by-2050.

IPCC (2018). *Global Warming of 1.5°C*. www.ipcc.ch/sr15.

Jacobsen, G. M., Choi, H., Turso, J. A., Johnsen, A. M., Bascom, A. J., Wei, X., & Olevsky, E. A. (2022). Fabrication and Characterization of Zirconium Silicide for Application to Gas-Cooled Fast Reactors. *Nuclear Technology*, *208*(1), 27–36. https://doi.org/10.1080/00295450.2021.1877504.

NEA (2022). *Meeting Climate Change Targets: The Role of Nuclear Energy*. OECD Publishing. www.oecd-nea.org/jcms/pl_69396/meeting-climate-change-targets-the-role-of-nuclear-energy.

Lemmon, E., Bell, I., Huber, M., & McLinden, M. (2022). Thermophysical Properties of Fluid Systems. In *NIST Chemistry WebBook, NIST Standard Reference Database Number 69*, Eds. P.J. Linstrom and W.G. Mallard, National Institute of Standards and Technology, Gaithersburg MD, 20899. https://doi.org/10.18434/T4D303.

Leppänen, J., Pusa, M., Viitanen, T., Valtavirta, V., & Kaltiaisenaho, T. (2015). The Serpent Monte Carlo code: Status, development and applications in 2013. *Annals of Nuclear Energy*, *82*, 142–150. https://doi.org/10.1016/J.ANUCENE.2014.08.024.

Lopez-Solis, R., & François, J.-L. (2018). The breed and burn nuclear reactor: A chronological, conceptual, and technological review. *International Journal of Energy Research*, *42*(3), 953–965. https://doi.org/10.1002/er.3854.

Pioro, I. L. (2016). Introduction. *In Handbook of Generation IV Nuclear Reactors* (pp. 37–54). Elsevier. https://doi.org/10.1016/B978-0-08-100149-3.00002-1.

Rodriguez, P., & Sundaram, C. V. (1981). Nuclear and materials aspects of the thorium fuel cycle. *Journal of Nuclear Materials*, *100*(1–3), 227–249. https://doi.org/10.1016/0022-3115(81)90534-1.

Schleicher, R. W., Choi, H., & Rawls, J. (2013). The Energy Multiplier Module: Advancing the Nuclear Fuel Cycle through Technology Innovations. *Nuclear Technology*, *184*(2), 169–180. https://doi.org/10.13182/NT13-A22313.

Zhou, X., Tang, Y., Lu, Z., Zhang, J., & Liu, B. (2017). Nuclear graphite for high temperature gas-cooled reactors. *New Carbon Materials*, *32*(3), 193–204. https://doi.org/10.1016/S1872-5805(17)60116-1.